Science Advances
AAAS

Supplementary Materials for

Van der Waals mid-wavelength infrared detector linear array for room temperature passive imaging

Tengfei Xu *et al.*

Corresponding author: Peng Wang, w_peng@mail.sitp.ac.cn; Weida Hu, wdhu@mail.sitp.ac.cn

Sci. Adv. **10**, eadn0560 (2024)
DOI: 10.1126/sciadv.adn0560

This PDF file includes:

Supplementary Text

Note 1. Fabrication of vdWs photodetector linear array

Fig. S1 presents the process of fabricating vdWs heterojunction photodetector linear array using the temperature-assisted sloping transfer method. The thin film materials are obtained through mechanical exfoliation. To protect these thin film materials, both the exfoliation and transfer processes are conducted inside a glovebox with an N_2 atmosphere.

The specific procedures for temperature-assisted sloping transfer method in Fig. S1 are as follows:

(**A**) Thin-layer MoS_2 are obtained from bulk material following mechanically exfoliation method, the tape is tightly adhered to polydimethylsiloxane (PDMS) and peeled off after 5 minutes. Some thin-layer MoS_2 materials are released from the tape and adhere to the PDMS, and then the MoS_2 with rectangular shape is transferred to a clean substrate. Further etching MoS_2 into sharp shapes using polymethyl methacrylate (PMMA) as a mask.

(**B**) The etched MoS_2 flake was transferred to another clean substrate using poly propylene carbonate (PPC) as the medium. The PPC is slowly released and heated to 50 ℃ until it is fully in contact with the target MoS_2. After being naturally cooled down to 30 ℃, the PPC is slowly lifted to stick the MoS_2.

(**C**) The PPC with the etched MoS_2 is slowly released onto another clean substrate and heated up to 120 ℃. Under the high temperature, the PPC melts and remains on the substrate. Finally, the PPC is removed in acetone.

(**D**) Similarly, a thin layer of BP material is obtained on the PDMS film. In order to minimize the formation of bubbles during the stacking process and ensure a smooth interface, the PDMS tilt angle is adjusted and gradually lowered, enabling the edges and corners of the BP to make initial contact with the MoS_2. Due to the different thermal expansion coefficients between polymers and inorganic materials, the contact interface between BP and MoS_2 gradually releases from one side to the other during heating to 35 ℃

(**E,F**) PMMA is spin-coated onto the silicon wafer, followed by patterning the electrodes using EBL. Cr/Au is then deposited sequentially using thermal evaporation to obtain custom electrodes of linear array device.

(**G**) The PMMA is spin-coated onto the silicon substrate again for masking purposes, and ebl is utilized to determine the etching windows.

(**H**) The exposed regions of the heterostructure are removed using reactive ion etching, resulting in the formation of independent linear array heterojunctions.

(**I**) By rinsing the device in acetone to remove excess PMMA, a van der Waals array photodetector can be obtained.

In addition, it is common practice to apply another layer of PMMA as a protective coating to prevent oxidation of the detector during the later testing process. EBL is then utilized to create windows in the electrode area.

Note 2. Theoretical calculations of density functional theory (DFT)

Our theoretical calculations were performed with Vienna Ab-initio Simulation Package (VASP)(*65*, *66*) using projector augmented wave (PAW) method(*67*). Exchange-correlation effects were taken into account by the Perdew-Burke-Ernzerhof (PBE) functional(*68*). The plane-wave cutoff energy was set to 520 eV. The structural relaxations were realized with energy and force convergence criteria of 10^{-5} eV and 0.01 eV/Å, respectively. To describe correctly the weak interactions, we used a semi-empirical correction scheme of DFT-D3(*69*) approach for PDMS/BP and BP/MoS_2 heterostructures. During optimization, first Brillouin zone of these materials was sampled with a Γ-centered mesh with reciprocal space resolution of $2\pi\times0.04$ $Å^{-1}$. In order to construct PDMS/BP and BP/MoS_2 stacking patterns with small lattice mismatch, we chose 1×1×1 unit cell of PDMS and 3×3×1 unit cells of monolayer BP, 1×4×1 unit cells of monolayer MoS_2 and 1×5×1 unit cells of monolayer BP, respectively. As shown in Fig. 1E(i), to determine the stability of systems, the adhesion energy of PDMS/BP and BP/MoS_2 are defined as E_{b1} and E_{b2}, as follows:

$E_{b1} = E_{PDMS/BP} - E_{PDMS} - E_{BP}$ $E_{b2} = E_{BP/MoS2} - E_{BP} - E_{MoS2}$

Here, $E_{PDMS/BP}$, $E_{BP/MoS2}$, E_{PDMS}, and E_{BP} and E_{MoS2} represent the energy of the PDMS/BP heterostructure, BP/MoS_2 heterostructure, isolated PDMS, BP, and MoS_2, respectively.

The adhesion energy of PDMS/BP and BP/MoS_2 without thermal expansion are calculated as E_{b1} = -0.4138 eV and E_{b2} = -0.7909 eV, respectively. Here, the larger the absolute value of adhesion energy, the higher the adhesion energy between the two materials. It is obvious that the adhesion energy between BP and MoS_2 is larger than that between BP and PDMS, indicating that BP is more likely to adhere to MoS_2 and separate from PDMS. This result also theoretically explains the previously reported direct use of PDMS-assisted transfer method to construct 2D material heterojunctions(*31*). However, it cannot be ignored that due to the viscous behavior of PDMS, removing PDMS requires overcoming the adhesion energy between PDMS and 2D materials, which inevitably causes damage to the stacked heterojunctions, such as bubbles and wrinkles. Previous studies have shown that the thermal expansion coefficients between polymers and inorganic materials differ by about 2 orders of magnitude, for example, the thermal expansion coefficient of PDMS is about 2×10^{-4} K^{-1} at room temperature(*42*), and thermal expansion coefficient of BP is about 10^{-6} order of magnitude at 293 K (*70*). This significant difference means that PDMS is more sensitive to temperature changes and its adhesion energy is easily affected. In our method, the temperature is generally raised from 25 °C to 35 °C. Therefore, during the heating process, the expansion of PDMS is much greater than that of BP. When a material is expands, its lattice structure will change, and the distance between atoms or molecules may increase or decrease. Because the adhesion process involves the interaction between surface atoms or molecules, the structural changes can affect the adhesion energy.

As shown in Fig. 1E(i), we applied biaxial tensile strain (+1% and +2%) equivalent to thermal expansion to the PDMS/BP to investigate the trend of changes in adhesion energy. As shown in Fig. 1E(ii), the adhesion energy of PDMS/BP shows a significant decrease trend (E_{b1}: from -0.4138 eV to -0.3904 eV, greater difference in adhesion energy with E_{b2}=-0.7909 eV), indicating the decrease in the adhesion force between PDMS and BP, making it easier for BP to separate from PDMS and form heterojunction with MoS_2. In addition, the removal of polymers may require smaller forces or lower energy to reduce the risk of damage, such as bubbles, wrinkles, or cracks, which is crucial for the uniformity of large-area heterojunctions.

Note 3. Analysis of the dark current for the pixels of the array

For a photodiode, the reverse current components include diffusion (Diff.) current, tunneling current (including trap-assisted tunneling (TAT) and band-to-band tunneling (BBT)), and Shockley-Read-Hall (SRH) current(*71*). Specifically, Diff. current is formed by electrons and holes excited thermally or optically diffusing along the energy band to the electrodes, BBT current is a tunneling current that electrons directly tunnel from the valence band to the conduction band while TAT current involves the indirect tunneling across the junction by way of intermediate trap. SRH current arises when electrons are excited to defect states near the middle of the depletion region and transition to the conduction band, forming a current collected by the electrode. In our work, the photodiode operates in the diffusion region at room temperature, where Diff. current is the main source of dark current. The current-voltage characteristic for an ideal diffusion-limited diode is given by

$$I_{\mathrm{D}}=AJ_{\mathrm{s}}[\exp(\frac{qV}{kT})-1]$$

Where A is the area, J_{s} is the saturation current density, q is the electron charge, V_{d} is the voltage, k is the Boltzmann constant, and T is the temperature. The saturation current density J_{s} can be expressed as

$$J_{\mathrm{s}}=\left(kT\right)^{1/2}n_i^2q^{1/2}[\frac{1}{p_{p0}}\left(\frac{\mu_e}{\tau_e}\right)^{1/2}+\frac{1}{n_{n0}}\left(\frac{\mu_h}{\tau_h}\right)^{1/2}]$$

where τ_e and τ_h the electron and hole lifetimes in the p-type and n-type regions, and p_{p0} and n_{n0} are the hole and electron majority carrier concentrations, respectively(*72*).

Previous studies have indicated that the thickness of two-dimensional materials affects the concentration of charge carriers. Taking MoS_2 as an example, the carrier concentration can vary by up to 10 times between single-layer and multi-layer MoS_2. Detailed thickness statistics from AFM reveal that the thickness of different pixels varies slightly, typically falling within the range of 85 to 94 nm. Consequently, for BP/MoS_2 pn junctions, differences in thickness lead to variations in carrier concentration, ultimately manifesting as differences in *I-V* current under both forward and reverse bias conditions. Moreover, the variation in carrier concentration distribution results in different depletion region potential barriers between pixels. Consequently, under high reverse bias voltages, significant band bending increases tunneling probabilities, altering the probabilities of tunneling currents, and amplifying current differences under reverse bias.

Note 4. Comparative analysis of *J-V* currents of arrays fabricated by our method and previous methods

To provide a more comprehensive analysis, as shown in Fig. S5, we statistically analyzed the *J-V* curves of arrayed devices fabricated using PDMS-assisted transfer method, PPC-assisted multiple-transfer method, PPC-assisted transfer method, and our temperature-assisted sloping transfer method.

The PDMS-assisted transfer method mainly keeps the material in a horizontal state, vertically pressing and lifting the PDMS to obtain a heterojunction. The loss of rectifying characteristics in various pixels may be related to the thickness of the heterojunctions. It is difficult to obtain materials with uniform thickness on a larger scale through mechanical exfoliation. For large-area heterojunctions, the rapid stacking transfer process leads to a more severe interface bubble phenomenon. Due to the viscous behavior of PDMS, the removal process may damage the heterojunction, and disrupt uniformity, leading to significant differences in *J-V* characteristics between pixels (Fig. S5A-up) and three orders of magnitude difference in the current density between pixels under a bias voltage of -1 V (Fig. S5A-down).

The PPC-assisted method allows for free picking and transfer of 2D materials. Therefore, we adopted two methods, including PPC-assisted multiple-transfer method of heterojunctions to the same substrate (Fig. S5B) and PPC-assisted transfer method of large-area heterojunction (Fig. S5C). For PPC-assisted multiple-transfer method in Fig. S5B, all pixels come from different materials, and the thickness cannot be consistent, which means that the carrier concentration and depletion region are different, exhibiting differences in *J-V* characteristics (Fig. S5B-up) two orders of magnitude difference in the current density under -1 V (Fig. S5B-down). As shown in Fig. S5C, the direct transfer method of large-area heterojunctions by PPC may improve the *J-V* performance. However, when the heterojunction is large or thick, the PPC melted on the substrate is prone to forming a certain step height difference near the edge of the heterojunction, which may lead to polymer fracture and residual issues. Although the current density between pixels is similar at -1 V (Fig. S5C-down), individual pixels exhibit different *J-V* characteristics, which may be related to polymer fracture and residual issues (Fig. S5C-up).

Our method benefits from the reduced adhesion energy, facilitating not only the release of BP but also minimizing damage to heterojunctions during polymer removal. This approach is effective for constructing uniform and smooth heterojunctions, where the approximate thickness ensures similar carrier concentrations and depletion potential barriers between pixels. All pixels exhibit similar rectification behavior (Fig. S5D-up) and *J-V* differences controlled within an order of magnitude (Fig. S5D-down), showing the smallest difference compared to other methods.

Note 5. Performance comparison of photodetector linear array fabricated by different methods

Figure S6A shows the *I-V* curve of the detector fabricated through multiple-transfer processes. It can be observed that the variations in material thickness due to the different materials used result in differences in electrical performance, leading to significant variations in the rectifying characteristics among these devices. Additionally, it can be noted that some devices did not exhibit rectifying characteristics, which can also be primarily attributed to variations in the thickness of MoS_2. As shown in Fig. S6B the thick MoS_2 gradually exhibits weak p-type behavior with increasing MoS_2 thickness(*73*), leading to a weaker potential barrier at the pn junction. This hinders the effective blocking of the transport of reverse bias downstream carriers, resulting in a weak rectification effect. The repeated release, heating, and dissolution processes of PPC in the multiple-transfer steps have significantly detrimental effects on the pre-existing heterojunctions on the substrate. Figure S6C demonstrates the blackbody D^* of the two types of photodetector linear arrays. The D^* the array devices obtained through multiple-transfer approaches is nearly on the order of 10^8 (blue region), with a significant performance gap between pixels. On the other hand, the blackbody D^* of the latter method (red region) is improved by an order of magnitude, reaching a level comparable to that of a single-pixel device.

Note 6. Comparison and discussion between our work and representative photodetector arrays based on TMDCs

Wavelength and blackbody response

TMDCs films for arrayed photodetectors are currently mainly grown directly through methods such as chemical vapor deposition (CVD)(*48*, *49*), metal-organic chemical vapor deposition (MOCVD)(*50*, *51*), molecular beam epitaxy (MBE)(*47*, *52*), tellurization(*18*), and selenization (*53*). These methods enable the efficient production of large-area TMDCs films. As listed in Table S1, detector arrays based on TMDCs typically feature larger pixel areas and larger array scales. For example, the pixel area of MoS_2/InGaAs heterojunctions grown by MBE can reach 300×300 μm^2(*51*), or the scale of array devices can be expanded to 16×16(*52*). However, TMDCs materials (MoS_2, $MoSe_2$, WS_2, and WSe_2) typically exhibit wide band gaps. The bandgaps of MoS_2 and WS_2 are relatively close, generally around 1.3 eV, and $MoTe_2$ is around 1.2 eV. Reported wavelength range of photoresponse is usually in the visible to short-wavelength infrared ranges. Noble metal dichalcogenides films are generally obtained through selenide or telluride noble metal films deposited by magnetron sputtering on of, so the scale of the films is sufficient to reach wafer level. For example, $PtTe_2$ has been able to achieve 4×4 array scale and stable laser response at 10.6 μm(*18*, *74*, *75*). The rich material system, wide band coverage, and efficient preparation methods for large-area thin films provide a good guarantee for achieving TMDCs photodetector arrays. However, the photoresponse of the implemented TMDCs photodetector arrays is from the laser source, and there are currently no reports of two-dimensional material detector arrays that achieve blackbody response. Simply put, lasers are monochromatic light with high energy density, and the radiation of blackbody is closely related to the temperature, including light waves of various wavelengths with lower energy density. Only a few infrared photodetectors based on quantum dots, carbon nanotubes, and BP have shown responses to blackbody radiation(*63*), and arrayed devices are even less reported.

In our work, we employ BP/MoS_2 as the primary device structure, using p-type narrow bandgap BP as the mid-infrared absorption layer and n-type MoS_2 as the contact layer. So far, the avenues for obtaining large-scale BP films are extremely limited, with the only effective means being mechanical exfoliation from bulk single crystals. Although there have been reports on BP film growth, it is still confined to relatively thick polycrystalline materials(*60*), making it challenging for high-performance detector arrays. In our work, to achieve a highly homogeneous infrared detector array with blackbody response, we opt to mechanically exfoliate BP and MoS_2 thin films from large single crystals. We employ heterojunction stacking as the primary method, optimizing the transfer process from the perspective of uniform interfaces. Ultimately, we achieve an average blackbody peak D^* of 2.34×10^9 $cm\cdot Hz^{1/2}\cdot W^{-1}$. Therefore, due to the size limitations imposed by mechanical exfoliation of materials, the scale of our arrayed device remains limited when compared to TMDCs arrayed devices. However, our current research approach for 2D vdWs heterostructure infrared detector array remains applicable. The epitaxial growth of high-quality 2D films is under investigation and the transfer of large-area vdWs heterostructures for arrayed devices will likely become an inevitable trend. The origins of dark current components remain similar, and the mechanism of photoelectric detection remains unchanged. Therefore, our work holds reference value for the long-term study of low-dimensional infrared detector arrays.

Imaging methods

As shown in Table S1, for TMDCs detector arrays, whether work in the visible or IR spectrum, the mainstream imaging method involves using laser-assisted illumination to image the mask pattern. This imaging method relies on actively emitted laser beams, using a mask with specific hollow patterns to block the incident laser, allowing the laser to pass only through the hollow part of mask onto the surface of array. That is to say, under the block of the mask, the light illuminated on the array has the same pattern with the mask. Finally, imaging information can be obtained by recording the current of the detector. Therefore, laser-assisted mask imaging method mainly depends on the block of the mask, and the imaging results usually can only present patterns similar to the mask, unable to record other information about the target. In addition, most TMDCs detector arrays typically image specific areas in a relatively fixed manner, rather than scanning along specific directions, so their imaging results are limited to simple patterns or letters composed of several pixels. At present, it has also been reported that a 1×10 $PtSe_2$/Ge array controlled by a stepper motor is used for scanning imaging(*53*), but its scanning range is relatively limited, and the imaging resolution is only 20×20 pixels. The final result is also a pattern similar to a hollow mask.

The push-broom passive imaging achieved in our work is used to image a blackbody like object. Any object above absolute zero in nature is radiating energy outward, and the radiated energy follows the Planck radiation distribution in accordance with Planck's law. The wavelength and power of external radiation from an object are related to its temperature. When the temperature of a blackbody changes, the radiation power and peak wavelength of radiation also change, providing us with the foundation for passive imaging. As shown in Fig. 4A in the manuscript, a glass-sealed U-shaped curved carbon fiber heating tube was employed as a blackbody-like radiation heat source, with the highest center temperature of the resistance wire around 1300 K. We use a len to focus light from the natural environment onto the detector array, and with the help of an 8-channel push-broom imaging system, record the position and collect photoelectric signals. Due to the signals from 8 pixels can be collected in parallel, while single-pixel imaging can only collect signals from 1 pixel at a time, the high-resolution imaging efficiency is directly increased by 8 times. Ultimately, we can directly map the collected signals on the computer to obtain passive imaging results, which provides more information compared to the commonly used laser-assisted mask imaging in TMDCs arrays.

Imaging results

The push-broom scanning passive imaging technology for 2D vdWs photodetector arrays can provide more resolution and imaging information compared to laser-assisted mask imaging method. The static laser-assisted mask imaging method has not fully realized the superiority of array scale, the imaging results only rely on the pixel information collected in a single acquisition. In this case, the imaging resolution is constrained by pixel density and array scale, making it difficult to achieve higher resolution imaging results. Push-broom scanning imaging technology for 8×1 vdWs detector array can alleviate the limitations of array scale on imaging resolution. Through periodic push and sweep actions, integrating and utilizing information between adjacent pixels, detector arrays can image areas within a certain range, achieving high-resolution imaging.

On the other hand, for TMDCs arrayed detectors, the core of their imaging lies in the patterning of the laser illuminated on the array by the masks. For pixels, there are only two situations, namely being illuminated by laser and not. Therefore, its imaging results can only show two

effects, bright and dark, and display patterns similar to the masks. In our work, the len only serves the purpose of focusing, and the irradiated light comes entirely from the signal radiated by the object itself in the environment. Therefore, the passive imaging results can directly reflect the information of the object in the real environment. As shown in Fig. 4D and Fig. 4E in the manuscript, the grayscale and flame images come from the same imaging results, with only the difference in color mapping. The heated U-shaped resistance wire can be significantly distinguished from the background environment, and the contour of the U-shaped wire can also be clearly displayed. In addition, the center temperature of the resistance wire is higher, while the surrounding temperature gradually decreases, resulting in the brightest area and a gradient phenomenon in the imaging. This temperature distribution pattern is consistent with Planck's radiation law, indicating that passive imaging technology can accurately reflect the temperature distribution of objects. After noise reduction processing, the imaging results further highlight these features. Firstly, the high temperature resistance wires form a clear boundary with the background, making them more clearly separated in the image and enhancing the visual perception of object contours. Secondly, temperature differences are clearly visible in the image. The resistance wire has a higher temperature and is the brightest in the image. The temperature on the periphery of the resistance wire is lower than the temperature at the center, appearing slightly bright. The lowest ambient background temperature is the darkest in the image. The color and brightness changes in different temperature regions are more pronounced, enhancing the perception of the distribution of object temperature. Although they are all about imaging methods of 2D arrayed devices, there are significant differences between the two imaging methods and their results. Unlike the patterns obtained from mask imaging, passive imaging provides more information about objects, backgrounds, and temperature distribution in natural scenes. Therefore, these two imaging methods correspond to the needs of different detecting scenes.

Note 7. Image non-uniformity correction for vdWs photodetector linear array

Uniformity correction is an image processing technique that eliminates the uneven brightness and contrast in an image, resulting in consistent brightness and contrast across the entire scene. In our work, considering the filtering effect and computational efficiency, we employed two methods for uniformity correction: mean filtering and Fast Fourier Transform (FFT) filtering. Among them, mean filtering is a linear filtering method where the values of the surrounding pixels are averaged to determine the value of the central pixel, helping to smooth the image. On the other hand, FFT filtering is based on Fourier transform analysis in the frequency domain. The filtered image is obtained by selectively removing or suppressing specific frequency components. The specific details of these two filtering methods are as follows:

Mean filtering

1. Grayscale conversion: Converting the original image into a grayscale image for subsequent processing.
2. Mean filtering: Applying a filter to the grayscale image to smooth irregular brightness variations.
3. Contrast stretching: Scaling the pixel values of the image using a linear transformation to enhance details and contrast.
4. Color mapping: Adding specific color mappings, such as a flame map, based on requirements to improve the visual appearance of the image.

Fast Fourier Transform filtering

1. Fast Fourier Transform: Transforming the original image from the spatial domain to the frequency domain.
2. Filtering: Perform filtering operations in the frequency domain by removing or suppressing specific frequency components.
3. Apply the inverse Fourier transform to the filtered frequency domain image, converting it back to the spatial domain.
4. Contrast stretching: Performing contrast enhancement on the image after inverse transformation.
5. Obtain the filtered image, which exhibits reduced or suppressed specific frequency components.

Note 8. Potential strategies to overcome the scaling limitations

For narrow bandgap 2D materials:

Large-scale single-crystal BP and Te should both be given priority consideration. Each of these materials possesses unique advantages. BP exhibits higher blackbody D^* in the mid-wavelength infrared range (typically around 10^9-10^{10}, compared to Te nanosheets at 10^8). BP is conducive to forming vdWs heterostructures with other layered materials to construct photodiodes, significantly reducing dark currents and improving sensitivity. The instability of BP is a major obstacle currently limiting its application in optoelectronic devices. Existing experimental and theoretical studies commonly believe that the instability is closely related to oxygen, water, and light(*62*). Particularly, the oxidation and decomposition processes of BP are significantly accelerated under illumination. However, the actual mechanisms of synergistic effects have not yet been clearly explained, making the study of the physical and chemical processes of BP oxidation increasingly crucial. Methods such as physical encapsulation and passivation, surface functionalization, and surface modification have been developed to enhance the stability(*76–79*). Common practices include covering the BP surface with a layer of aluminum oxide or boron nitride or using spin-coated polymers for physical isolation. Additionally, passivation or modification of BP with organic molecules or metal atoms has also proven to be a convenient and effective method. These stabilization techniques can temporarily extend the lifespan of BP while maintaining its optoelectronic properties. Future research should continue to explore material engineering or novel chemical treatment methods to extend environmental stability, making it more suitable for long-term applications in optoelectronic devices. Research into this issue is expected to reveal new physical phenomena and chemical laws, providing a theoretical foundation and technical support for the passivation of two-dimensional materials.

Large-area single-crystal BP films are essential for the development of larger-scale arrayed devices. Currently, layered BP is primarily obtained through mechanical exfoliation from bulk materials. This top-down approach typically produces samples with higher crystal quality and exhibits excellent electronic and optical performance, making it particularly suitable for the development of prototype optoelectronic devices. However, mechanical exfoliation usually relies on manual operations, and the materials prepared often lack consistency in size, thickness, and shape, which is unacceptable for the development and application of large-scale arrayed devices requiring high sensitivity and consistency. Therefore, developing methods for exfoliating large-area uniform films becomes especially important. The reported large-area mechanical exfoliation and transfer methods for materials like graphene and transition metal dichalcogenides (TMDCs), given the similar structural characteristics of black phosphorus, suggest that improved and scalable techniques for larger-area BP films are feasible. It is necessary to comprehensively consider the physical and chemical stability of BP films during the exfoliation and integration process, such as material damage, control of scale and thickness, interface fundamentals, mechanical stress, and contamination. For instance, improper interface contact could reduce carrier transport efficiency, while residues from polymers and contamination from organic solvents could affect the electrochemical stability and photoresponse of the material. Inappropriate release of mechanical stress may introduce micro-cracks or other structural defects, further reducing the material's reliability and lifespan.

Due to the unique structure of the black phosphorus (BP) phase, simultaneous research and development of epitaxial growth techniques for single-crystal thin films are particularly crucial for breaking through the scalability limitations of BP array devices. Further research is needed in deposition techniques and nucleation principles to achieve large-area, uniform, high-quality BP

thin films. Additionally, the ability to integrate these single-crystal films into existing semiconductor processes can greatly expand the potential applications of BP, especially in optoelectronic technologies. Progress has also been reported in the study of Te materials. Te grown under specific conditions has demonstrated excellent sensitivity in the infrared range, making Te a material system with tremendous potential, especially in mid-wavelength infrared detection. Te can maintain a relatively stable state in the air without oxidation. There have been reports on both n-type and p-type characteristics of Te(*63*, *80*), providing flexibility in direct or separately grown and transferred structures, and offering a richer design space for constructing homogeneous photovoltaic devices. Moreover, focusing solely on the absorber layer material is far from sufficient. Constructing photodiode array devices also requires addressing the growth of the contact layer material and involves methods for building heterojunction structures, whether through scalable transfer techniques or direct heteroepitaxy. This process may be a long-term, gradual resolution for the entire research field.

In summary, the unique properties of BP and Te make them ideal choices for mid-wavelength infrared photodetectors, providing reliable and efficient solutions for mid-wavelength infrared imaging and sensing applications. Future research directions will focus on achieving large-scale single-crystal growth of BP and Te, followed by the study of focal plane array devices, addressing key scientific issues during this process, and subsequently breaking through critical technologies, which is imminent soon.

For wide bandgap TMDCs materials:

Ultra-thin wafer-scale TMDCs materials are beneficial for achieving high-performance electronic devices. However, for optoelectronic detectors, such as MoS_2, when the layer is too thin, light absorption is reduced on one hand, and the common S vacancies causing defect states will affect the photoelectric process, diminishing the detector's performance. To further increase the thickness and scale of TMDCs materials' epitaxial growth, we believe it is essential to delve deeper into the growth mechanism, thoroughly analyzing the principles of TMDCs material growth. This includes understanding reaction kinetics, surface diffusion, and gas-phase transport under various growth conditions. The research strategy primarily focuses on breaking through in single-layer material achievement initially, gradually extending to the controllability study of multi-layer materials, aiming for the growth of single-crystal films. Current trends indicate progress in this direction, with reports on monolayer, bilayer, and multi-layer TMDCs materials(*45*, *81*, *82*).

Supplementary Table

Table S1 Comparison of arrayed photodetectors based on 2D materials.

Devices		Blackbody sensitive	Fill-factor	Wavelengths	Function	Ref.
8×1	BP/MoS_2	Yes	~77%	MWIR ($\lambda_{cut\text{-}off}$ = 3.8 μm)	Push-broom scannning passive imaging	This work
1×4	Te/Graphene	Yes	~64%	MWIR ($\lambda_{cut\text{-}off}$ = 3 μm)	-	(*83*)
7×8	Graphene/MoS_2/Graphene	-	-	405~904 nm	Laser-assisted mask imaging	(*50*)
5×5	MoS_2/$In_{0.53}Ga_{0.47}As$	-	-	405~1550 nm	Laser-assisted mask imaging	(*51*)
8×8	MoS_2	-	-	405~638 nm	Laser-assisted mask imaging	(*15*)
10×10	MoS_2	-	-	520 nm	Laser-assisted mask imaging	(*16*)
4×4	$MoSe_2$/Si	-	~32%	360~1550 nm	Laser-assisted mask imaging	(*84*)
8×8	$MoSe_2$	-	-	450~785 nm	Laser-assisted mask imaging	(*48*)
6×6	WS_2	-	-	405~852 nm	Laser-assisted mask imaging	(*49*)
6×10	WSe_2/Graphene	-	-	450~633 nm	Laser-assisted mask imaging	(*85*)
6×6	WSe_2	-	-	445~635 nm	Laser-assisted mask imaging	(*86*)
16×1	GaSe/GaSb	-	-	637~1550 nm	Passive imaging	(*47*)
16×16	GaSe/Graphene	-	-	532 nm	Light-assisted mask imaging	(*52*)
4×4	$GeSe_2$/GaN	-	~32%	205~400 nm	Laser-assisted mask imaging	(*74*)
4×4	$PtTe_2$/Si	-	-	808 nm~10.6 μm	Laser-assisted mask imaging	(*18*)
8×8	$PtTe_2$/Si	-	~16%	200~1200 nm	Laser-assisted mask imaging	(*75*)
1×10	$PtSe_2$/Ge	-	-	400~2200 nm	Laser-assisted mask imaging	(*53*)
4×4	Ga_2O_3	-	~7%	$\lambda_{cut\text{-}off}$=265 nm	Laser-assisted mask imaging	(*87*)
10×10	$(PMA)_2FAPb_2I_7$	-	~6%	405~904 nm	Laser-assisted mask imaging	(*88*)
12×11	$(BA)_2PbI_4$	-	-	405~1550 nm	Laser-assisted mask imaging	(*89*)
8×8	$MAPbI_3$/Si	-	~16%	405~638 nm	Laser-assisted mask imaging	(*90*)

Figures

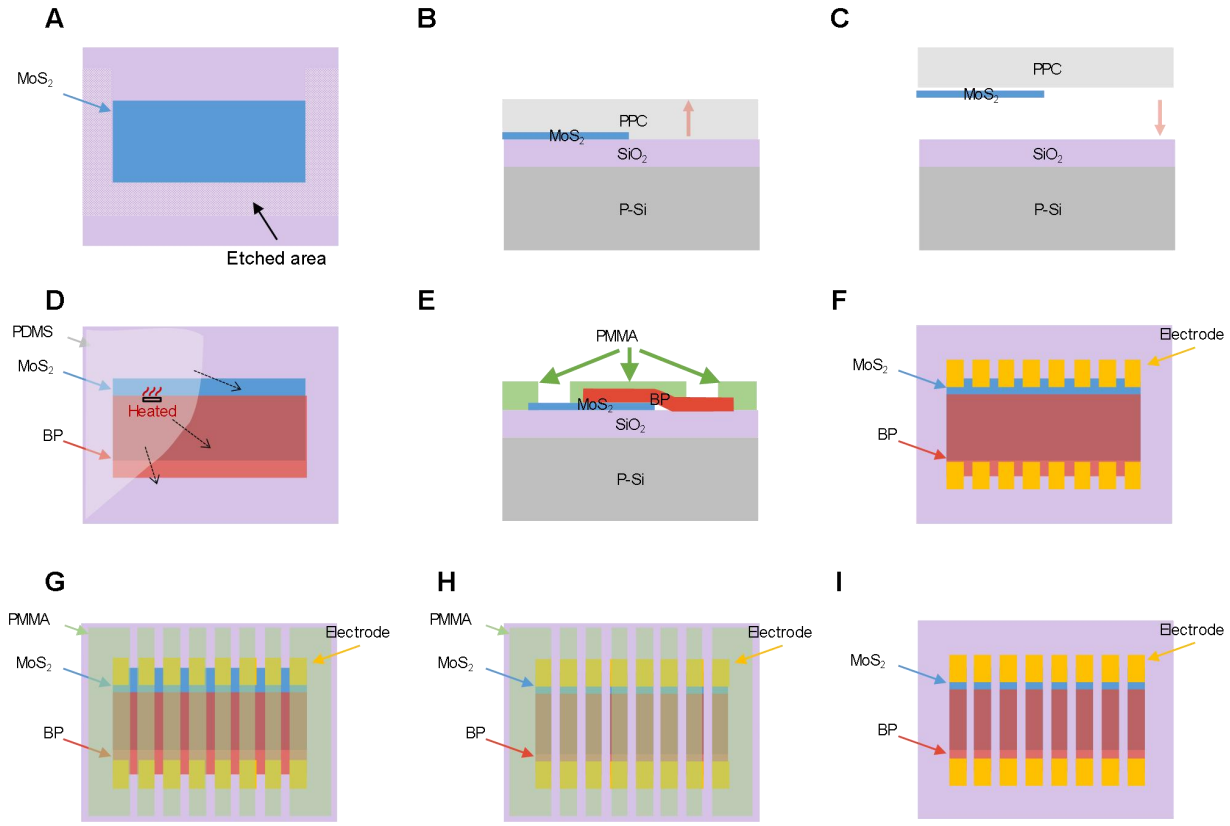

Fig. S1. Schematic diagram of the temperature-assisted sloping transfer method for vdWs photodetector linear array.

(**A**) Etching MoS_2 into sharp shapes using polymethyl methacrylate (PMMA) as a mask.
(**B**) Using poly propylene carbonate (PPC) as the medium to pick up the eched MoS_2.
(**C**) Transfer the etched MoS_2 onto another clean substrate.
(**D**) Using the temperature-assisted sloping transfer method to transfer and stack BP onto MoS_2.
(**E**) PMMA is spin-coated onto the silicon wafer, followed by patterning the electrodes using EBL.
(**F**) Electrodes obtained by thermal evaporation.
(**G**) The PMMA is spin-coated again for masking purposes.
(**H**) The exposed regions of the heterostructure are removed using reactive ion etching.
(**I**) Rinsing the device in acetone to remove PMMA.
The details have been described in Supplementary Text Note 1.

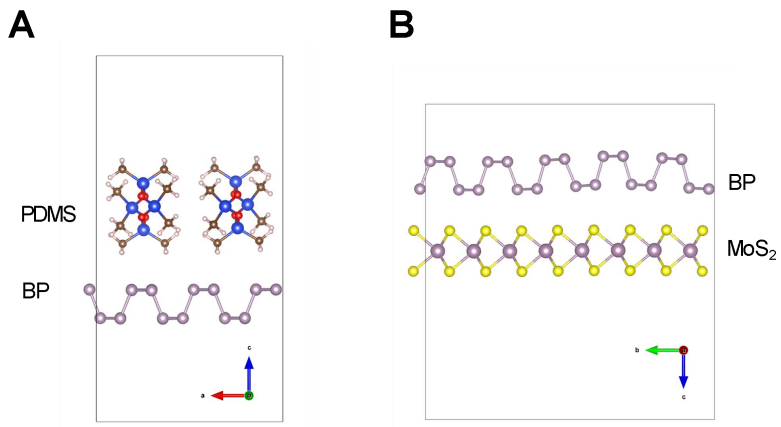

Fig. S2. The structures of PDMS/BP (A) and BP/MoS_2 (B) for DFT calculations.

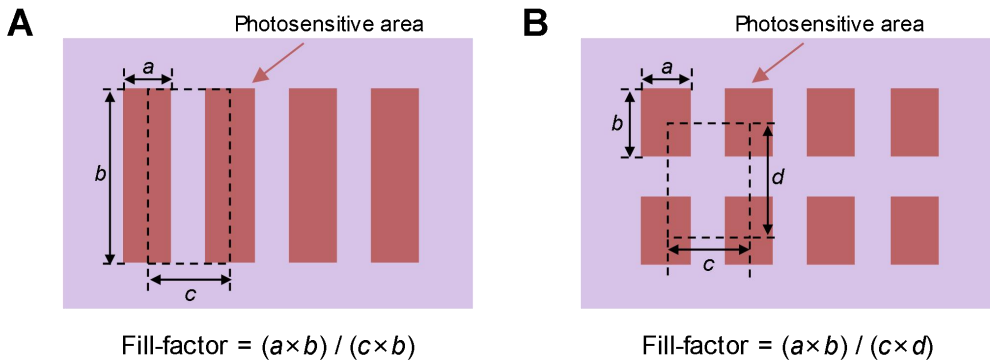

Fig. S3. Calculation method for the fill-factor of linear array (A) and array devices (B).

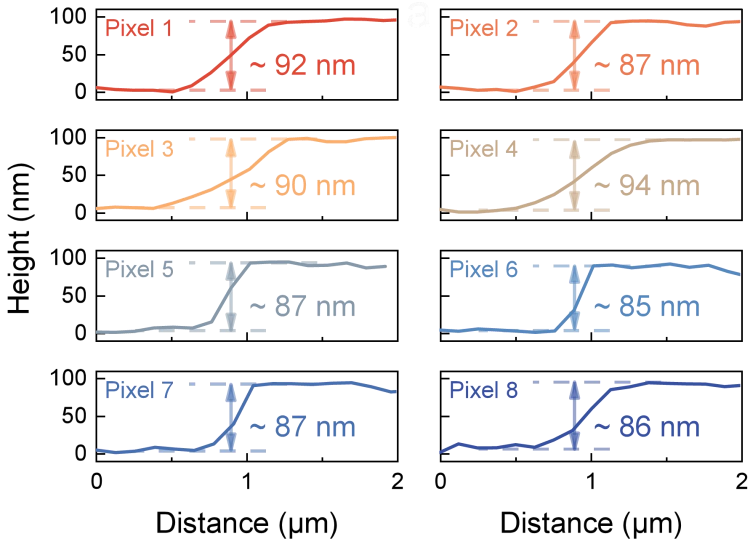

Fig. S4. Thickness of all pixels of the linear photodetector array obtained by AFM.

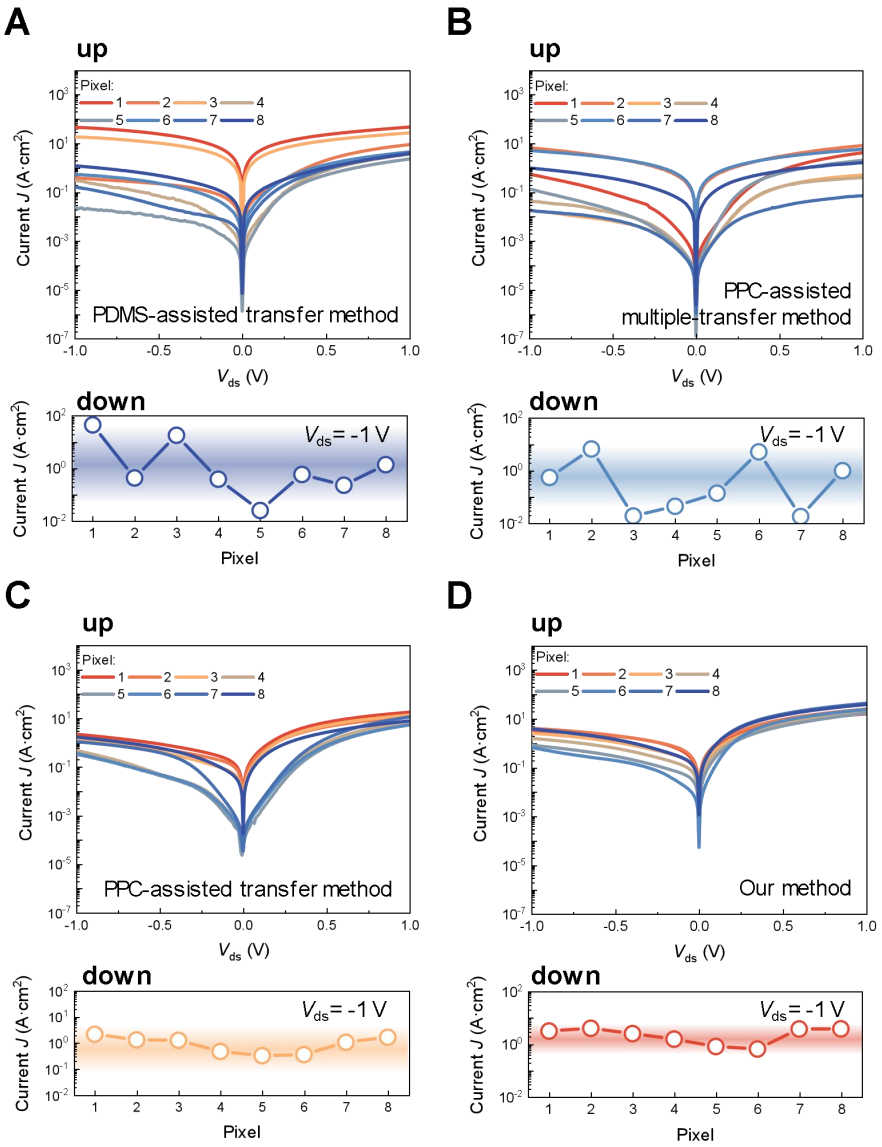

Fig. S5. *J-V* curves (up) and current density under bias of -1 V (down) of the linear array prepared by different methods. (**A**) PDMS-assisted transfer method, (**B**) PPC-assisted multiple-transfer method, (**C**) PPC-assisted transfer method, and (**D**) our temperature-assisted sloping transfer method.

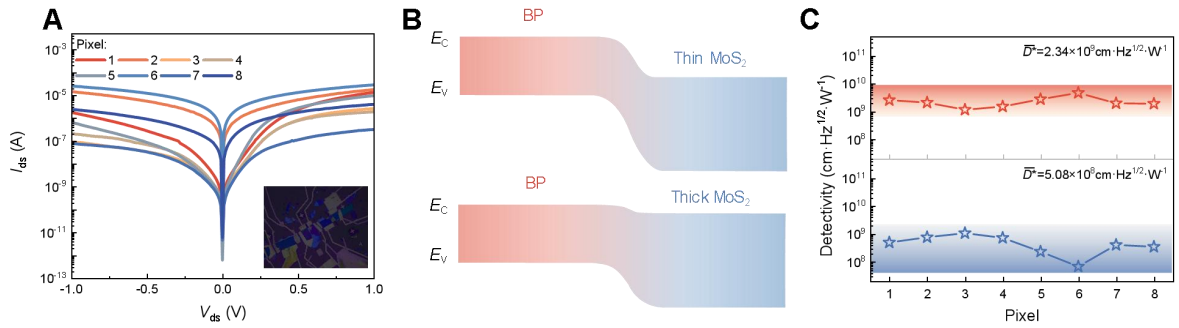

Fig. S6. Characterization of vdWs photodetector linear array. (**A**) *I-V* curves of the photodetector linear array fabricated by PPC-assisted multiple-transfer method. Inset: Optical microscope photograph of the linear array. (**B**) The thickness of MoS_2 causes changes in the band structure of the BP/MoS_2 pn junction. (**C**) The peak detectivity D^* and average peak detectivity D^* for the array devices fabricated by these two methods were evaluated at a blackbody temperature of 1,173 K.

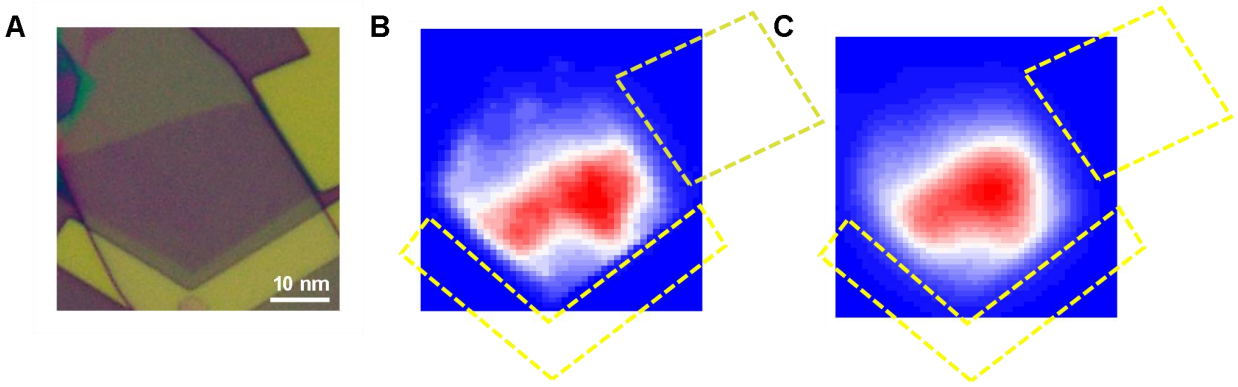

Fig. S7. Scanning photocurrent microscope mapping measurement of the photodiode using visible and infrared laser as sources. (**A**) Optical microscope photograph of the single-pixel BP/MoS_2 photodiode with sharp edges. (**B**,**C**) Scanning photocurrent microscope mapping measurement under 637 nm (B) and 2 μm (C) laser illumination.

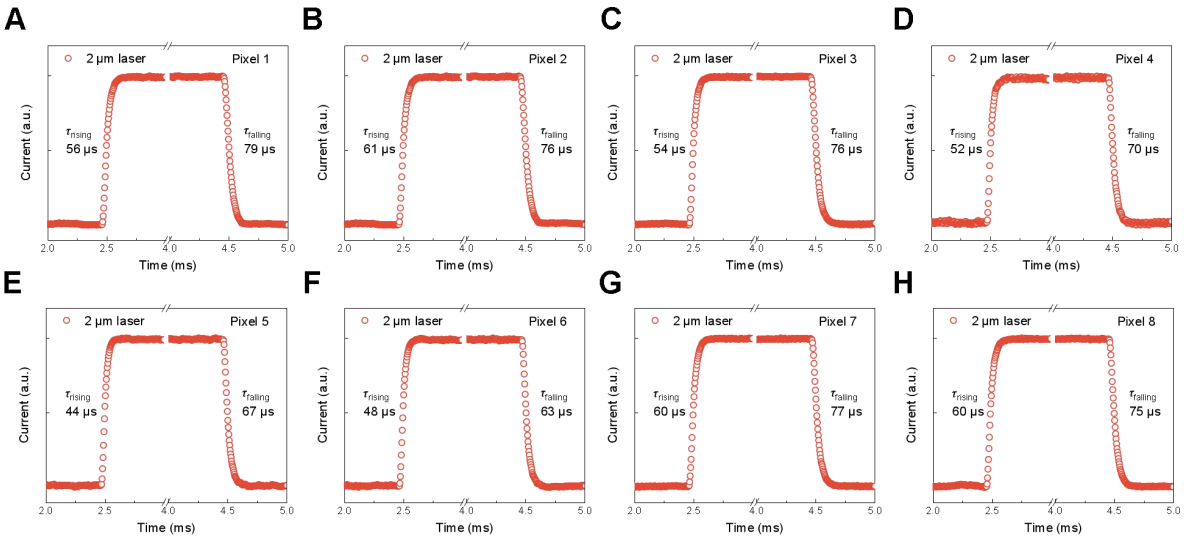

Fig. S8. Time-resolved photoresponse of all pixels in the photodetector linear array at 2 μm.
(**A**) Response time of pixel 1.
(**B**) Response time of pixel 2.
(**C**) Response time of pixel 3.
(**D**) Response time of pixel 4.
(**E**) Response time of pixel 5.
(**F**) Response time of pixel 6.
(**G**) Response time of pixel 7.
(**H**) Response time of pixel 8.

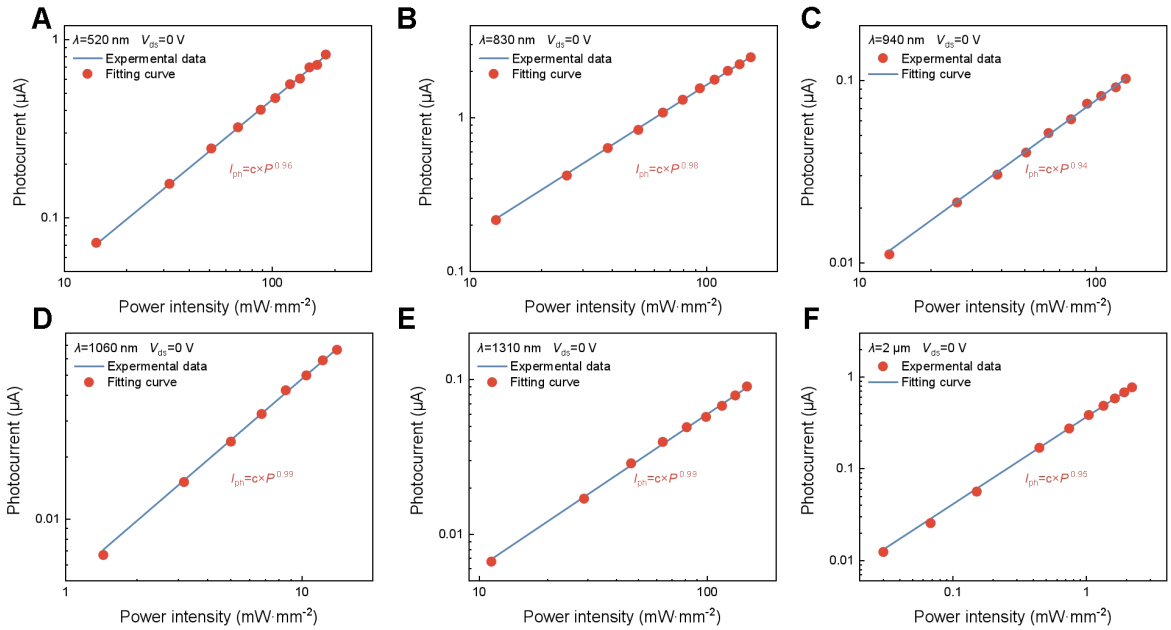

Fig. S9. Power dependence of the BP/MoS_2 vdWs photodetector photocurrent under laser illumination with different wavelengths.

(**A**) Power dependence of photocurrent under 520 nm.
(**B**) Power dependence of photocurrent under 830 nm.
(**C**) Power dependence of photocurrent under 940 nm.
(**D**) Power dependence of photocurrent under 1060 nm.
(**E**) Power dependence of photocurrent under 1310 nm.
(**F**) Power dependence of photocurrent under 2 μm.

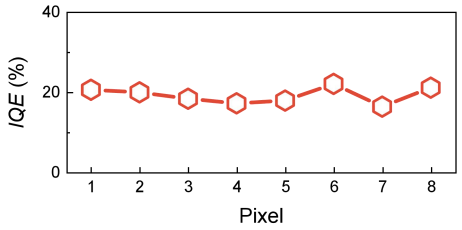

Fig. S10. The *IQE* of all the responsive pixels with 2 μm laser as the source.

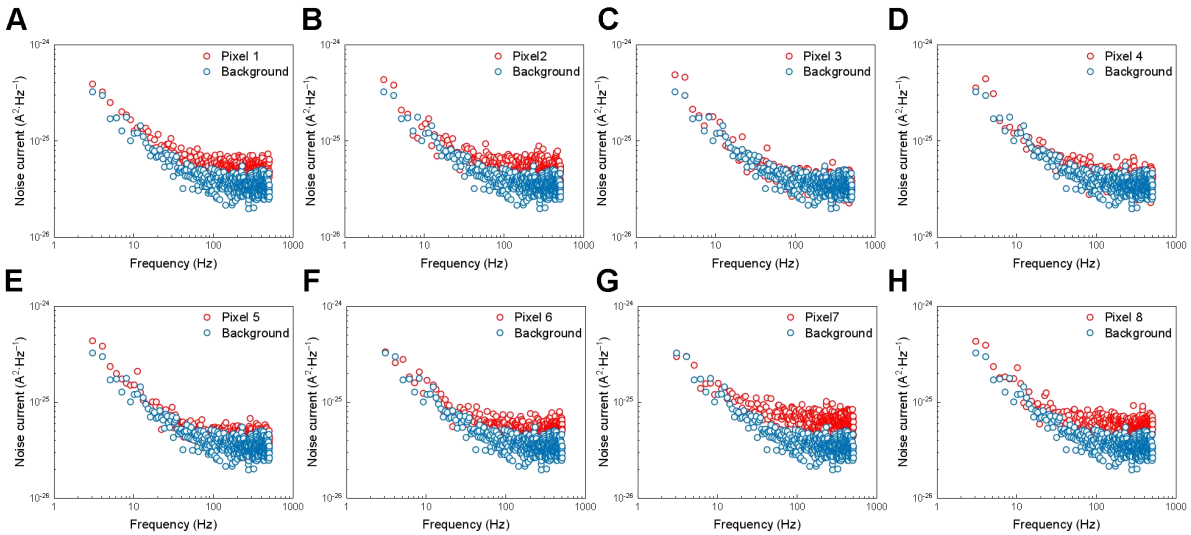

Fig. S11. Spectral noise current of all pixels of the photodetector linear array and the background.

(**A**) Spectral noise current of pixel 1.
(**B**) Spectral noise current of pixel 2.
(**C**) Spectral noise current of pixel 3.
(**D**) Spectral noise current of pixel 4.
(**E**) Spectral noise current of pixel 5.
(**F**) Spectral noise current of pixel 6.
(**G**) Spectral noise current of pixel 7.
(**H**) Spectral noise current of pixel 8.

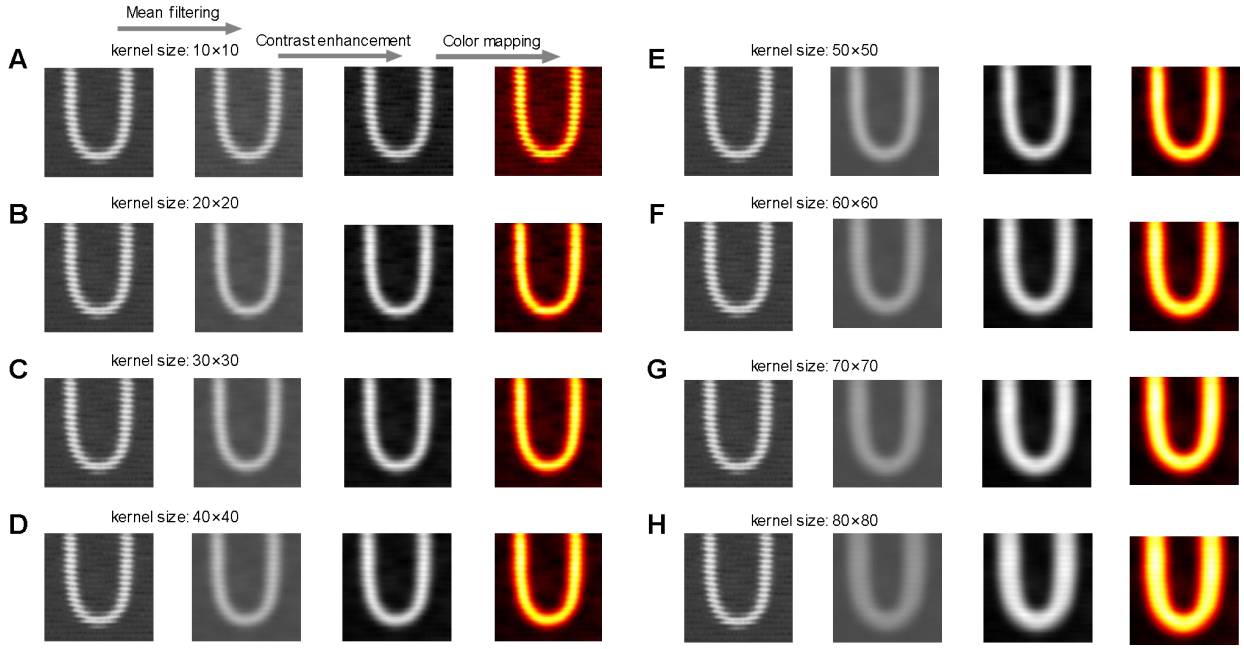

Fig. S12. Image non-uniformity correction using mean filtering with different kernel sizes. Four images in each group, from left to right, are original image by push-broom scanning passive imaging, image after mean filtering, image after contrast enhancement, and image after flame map mapping, respectively.

(**A**) Kernel size of mean filtering is set to 10×10.
(**B**) Kernel size of mean filtering is set to 20×20.
(**C**) Kernel size of mean filtering is set to 30×30.
(**D**) Kernel size of mean filtering is set to 40×40.
(**E**) Kernel size of mean filtering is set to 50×50.
(**F**) Kernel size of mean filtering is set to 60×60.
(**G**) Kernel size of mean filtering is set to 70×70.
(**H**) Kernel size of mean filtering is set to 80×80.
The details have been described in Supplementary Text Note 7.

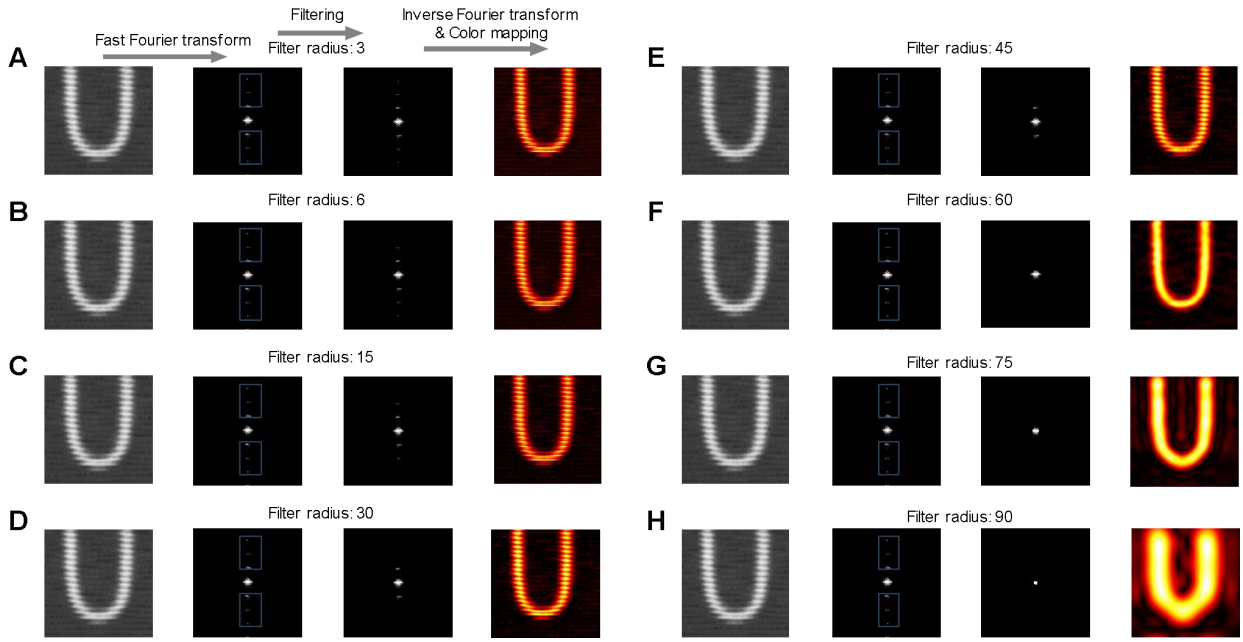

Fig. S13. Image non-uniformity correction using FFT filtering with different radii.
Four images in each group, from left to right, are original image by push-broom scanning passive imaging, image fast Fourier transform, image after filtering, and image after inverse Fourier transform and flame map mapping, respectively.
(**A**) Radius of FFT filtering is set to 3.
(**B**) Radius of FFT filtering is set to 6.
(**C**) Radius of FFT filtering is set to 15.
(**D**) Radius of FFT filtering is set to 30.
(**E**) Radius of FFT filtering is set to 45.
(**F**) Radius of FFT filtering is set to 60.
(**G**) Radius of FFT filtering is set to 75.
(**H**) Radius of FFT filtering is set to 90.
The details have been described in Supplementary Text Note 7.

REFERENCES AND NOTES

1. F. Xia, H. Wang, D. Xiao, M. Dubey, A. Ramasubramaniam, Two-dimensional material nanophotonics. *Nat. Photonics* **8**, 899–907 (2014).

2. F. H. L. Koppens, T. Mueller, Ph. Avouris, A. C. Ferrari, M. S. Vitiello, M. Polini, Photodetectors based on graphene, other two-dimensional materials and hybrid systems. *Nat. Nanotechnol.* **9**, 780–793 (2014).

3. N. Huo, G. Konstantatos, Recent progress and future prospects of 2D-based photodetectors. *Adv. Mater.* **30**, e1801164 (2018).

4. A. Soibel, D. Z. Ting, C. J. Hill, A. M. Fisher, L. Hoglund, S. A. Keo, S. D. Gunapala, Mid-wavelength infrared InAsSb/InSb nBn detector with extended cut-off wavelength. *Appl. Phys. Lett.* **109**, 103505 (2016).

5. Y. Wang, Y. Gu, A. Cui, Q. Li, T. He, K. Zhang, Z. Wang, Z. Li, Z. Zhang, P. Wu, R. Xie, F. Wang, P. Wang, C. Shan, H. Li, Z. Ye, P. Zhou, W. Hu, Fast uncooled mid-wavelength infrared photodetectors with heterostructures of van der Waals on epitaxial HgCdTe. *Adv. Mater.* **34**, e2107772 (2022).

6. D. Alshahrani, M. Kesaria, J. J. Jiménez, D. Kwan, V. Srivastava, M. Delmas, F. M. Morales, B. Liang, D. Huffaker, Effect of interfacial schemes on the optical and structural properties of InAs/GaSb type-II superlattices. *ACS Appl. Mater. Interfaces* **15**, 8624–8635 (2023).

7. A. Rogalski, Progress in focal plane array technologies. *Prog. Quantum Electron.* **36**, 342–473 (2012).

8. Y. Xie, B. Zhang, S. Wang, D. Wang, A. Wang, Z. Wang, H. Yu, H. Zhang, Y. Chen, M. Zhao, B. Huang, L. Mei, J. Wang, Ultrabroadband MoS2 photodetector with spectral response from 445 to 2717 nm. *Adv. Mater.* **29**, 1605972 (2017).

9. W. Li, L. Liu, Q. Tao, Y. Chen, Z. Lu, L. Kong, W. Dang, W. Zhang, Z. Li, Q. Li, J. Tang, L. Ren, W. Song, X. Duan, C. Ma, Y. Xiang, L. Liao, Y. Liu, Realization of ultra-scaled MoS2 vertical diodes via double-side electrodes lamination. *Nano Lett.* **22**, 4429, 4436(2022).

10. N. Huo, G. Konstantatos, Ultrasensitive all-2D MoS2 phototransistors enabled by an out-of-plane MoS2 PN homojunction. *Nat. Commun.* **8**, 572 (2017).

11. F. Zhong, J. Ye, T. He, L. Zhang, Z. Wang, Q. Li, B. Han, P. Wang, P. Wu, Y. Yu, J. Guo, Z. Zhang, M. Peng, T. Xu, X. Ge, Y. Wang, H. Wang, M. Zubair, X. Zhou, P. Gao, Z. Fan, W. Hu, Substitutionally doped MoSe2 for high-performance electronics and optoelectronics. *Small* **17**, e2102855 (2021).

12. A. Varghese, D. Saha, K. Thakar, V. Jindal, S. Ghosh, N. V. Medhekar, S. Ghosh, S. Lodha, Near-direct bandgap WSe2/ReS2 type-II pn heterojunction for enhanced ultrafast photodetection and high-performance photovoltaics. *Nano Lett.* **20**, 1707–1717 (2020).

13. D. Jariwala, V. K. Sangwan, C.-C. Wu, P. L. Prabhumirashi, M. L. Geier, T. J. Marks, L. J. Lauhon, M. C. Hersam, Gate-tunable carbon nanotube–MoS2 heterojunction p-n diode. *Proc. Natl. Acad. Sci. U.S.A.* **110**, 18076–18080 (2013).

14. Y. Wen, L. Yin, P. He, Z. Wang, X. Zhang, Q. Wang, T. A. Shifa, K. Xu, F. Wang, X. Zhan, F. Wang, C. Jiang, J. He, Integrated high-performance infrared phototransistor arrays composed of nonlayered PbS–MoS2 heterostructures with edge contacts. *Nano Lett.* **16**, 6437–6444 (2016).

15. S. Hong, N. Zagni, S. Choo, N. Liu, S. Baek, A. Bala, H. Yoo, B. H. Kang, H. J. Kim, H. J. Yun, M. A. Alam, S. Kim, Highly sensitive active pixel image sensor array driven by large-area bilayer MoS2 transistor circuitry. *Nat. Commun.* **12**, 3559 (2021).

16. B. Sun, L. Kong, G. Li, Q. Su, X. Zhang, Z. Liu, Y. Peng, G. Liao, T. Shi, Fully integrated photodetector array based on an electrochemically exfoliated, atomically thin MoS2 film for photoimaging. *ACS Appl. Electron. Mater.* **4**, 1010–1018 (2022).

17. Q. Zhu, Y. Chen, X. Zhu, Y. Sun, Z. Cheng, J. Xu, M. Xu, High-performance near-infrared PtSe2/n-Ge heterojunction photodetector with ultrathin Al2O3 passivation interlayer. *Sci. China Mater.* **66**, 2777–2787 (2023).

18. L. Zeng, D. Wu, J. Jie, X. Ren, X. Hu, S. P. Lau, Y. Chai, Y. H. Tsang, Van der Waals epitaxial growth of mosaic-like 2D platinum ditelluride layers for room-temperature mid-infrared photodetection up to 10.6 μm. *Adv. Mater.* **32**, e2004412 (2020).

19. L. Li, Y. Yu, G. J. Ye, Q. Ge, X. Ou, H. Wu, D. Feng, X. H. Chen, Y. Zhang, Black phosphorus field-effect transistors. *Nat. Nanotechnol.* **9**, 372–377 (2014).

20. M. Amani, E. Regan, J. Bullock, G. H. Ahn, A. Javey, Mid-wave infrared photoconductors based on black phosphorus-arsenic alloys. *ACS Nano* **11**, 11724–11731 (2017).

21. H. Yuan, X. Liu, F. Afshinmanesh, W. Li, G. Xu, J. Sun, B. Lian, A. G. Curto, G. Ye, Y. Hikita, Z. Shen, S.-C. Zhang, X. Chen, M. Brongersma, H. Y. Hwang, Y. Cui, Polarization-sensitive broadband photodetector using a black phosphorus vertical p–n junction. *Nat. Nanotechnol.* **10**, 707–713 (2015).

22. J. Bullock, M. Amani, J. Cho, Y.-Z. Chen, G. H. Ahn, V. Adinolfi, V. R. Shrestha, Y. Gao, K. B. Crozier, Y.-L. Chueh, A. Javey, Polarization-resolved black phosphorus/molybdenum disulfide mid-wave infrared photodiodes with high detectivity at room temperature. *Nat. Photonics* **12**, 601–607 (2018).

23. L. Ye, P. Wang, W. Luo, F. Gong, L. Liao, T. Liu, L. Tong, J. Zang, J. Xu, W. Hu, Highly polarization sensitive infrared photodetector based on black phosphorus-on-WSe2 photogate vertical heterostructure. *Nano Energy* **37**, 53–60 (2017).

24. S. Lee, R. Peng, C. Wu, M. Li, Programmable black phosphorus image sensor for broadband optoelectronic edge computing. *Nat. Commun.* **13**, 1485 (2022).

25. H. Kim, S. Z. Uddin, D.-H. Lien, M. Yeh, N. S. Azar, S. Balendhran, T. Kim, N. Gupta, Y. Rho, C. P. Grigoropoulos, K. B. Crozier, A. Javey, Actively variable-spectrum optoelectronics with black phosphorus. *Nature* **596**, 232–237 (2021).

26. S. Yuan, D. Naveh, K. Watanabe, T. Taniguchi, F. Xia, A wavelength-scale black phosphorus spectrometer. *Nat. Photonics* **15**, 601–607 (2021).

27. Y. Chen, Y. Wang, Z. Wang, Y. Gu, Y. Ye, X. Chai, J. Ye, Y. Chen, R. Xie, Y. Zhou, Z. Hu, Q. Li, L. Zhang, F. Wang, P. Wang, J. Miao, J. Wang, X. Chen, W. Lu, P. Zhou, W. Hu, Unipolar barrier photodetectors based on van der Waals heterostructures. *Nat. Electron.* **4**, 357–363 (2021).

28. P. Wu, L. Ye, L. Tong, P. Wang, Y. Wang, H. Wang, H. Ge, Z. Wang, Y. Gu, K. Zhang, Y. Yu, M. Peng, F. Wang, M. Huang, P. Zhou, W. Hu, Van der Waals two-color infrared photodetector. *Light Sci. Appl.* **11**, 6 (2022).

29. L. Ye, H. Li, Z. Chen, J. Xu, Near-infrared photodetector based on MoS2/black phosphorus heterojunction. *ACS Photonics* **3**, 692–699 (2016).

30. C. R. Dean, A. F. Young, I. Meric, C. Lee, L. Wang, S. Sorgenfrei, K. Watanabe, T. Taniguchi, P. Kim, K. L. Shepard, J. Hone, Boron nitride substrates for high-quality graphene electronics. *Nat. Nanotechnol.* **5**, 722–726 (2010).

31. H. Jawa, A. Varghese, S. Ghosh, S. Sahoo, Y. Yin, N. V. Medhekar, S. Lodha, Wavelength-controlled photocurrent polarity switching in BP-MoS2 heterostructure. *Adv. Funct. Mater.* **32**, 2112696 (2022).

32. X. Chen, X. Lu, B. Deng, O. Sinai, Y. Shao, C. Li, S. Yuan, V. Tran, K. Watanabe, T. Taniguchi, D. Naveh, L. Yang, F. Xia, Widely tunable black phosphorus mid-infrared photodetector. *Nat. Commun.* **8**, 1672 (2017).

33. L. Tao, H. Li, Y. Gao, Z. Chen, L. Wang, Y. Deng, J. Zhang, J. Xu, Deterministic and etching-free transfer of large-scale 2D layered materials for constructing interlayer coupled van der Waals heterostructures. *Adv. Mater. Technol.* **3**, 1700282 (2018).

34. D. G. Purdie, N. M. Pugno, T. Taniguchi, K. Watanabe, A. C. Ferrari, A. Lombardo, Cleaning interfaces in layered materials heterostructures. *Nat. Commun.* **9**, 5387 (2018).

35. K. Kinoshita, R. Moriya, M. Onodera, Y. Wakafuji, S. Masubuchi, K. Watanabe, T. Taniguchi, T. Machida, Dry release transfer of graphene and few-layer h-BN by utilizing thermoplasticity of polypropylene carbonate. *NPJ 2D Mater. Appl.* **3**, 22 (2019).

36. T. Iwasaki, K. Endo, E. Watanabe, D. Tsuya, Y. Morita, S. Nakaharai, Y. Noguchi, Y. Wakayama, K. Watanabe, T. Taniguchi, S. Moriyama, Bubble-free transfer technique for high-quality graphene/hexagonal boron nitride van der Waals heterostructures. *ACS Appl. Mater. Interfaces* **12**, 8533–8538 (2020).

37. J. Chen, L. Liu, H. Chen, N. Xu, S. Deng, Controlled preparation of high quality bubble-free and uniform conducting interfaces of vertical van der Waals heterostructures of arrays. *ACS Appl. Mater. Interfaces* **16**, 10877–10885 (2024).

38. F. Wang, T. Zhang, R. Xie, Z. Wang, W. Hu, How to characterize figures of merit of two-dimensional photodetectors. *Nat. Commun.* **14**, 2224 (2023).

39. G.-X. Ni, Y. Zheng, S. Bae, H. R. Kim, A. Pachoud, Y. S. Kim, C.-L. Tan, D. Im, J.-H. Ahn, B. H. Hong, B. Özyilmaz, Quasi-periodic nanoripples in graphene grown by chemical vapor deposition and its impact on charge transport. *ACS Nano* **6**, 1158–1164 (2012).

40. H. Fang, W. Hu, Photogating in low dimensional photodetectors. *Adv. Sci.* **4**, 1700323 (2017).

41. Y. Liu, S. Liu, Z. Wang, B. Li, K. Watanabe, T. Taniguchi, W. J. Yoo, J. Hone, Low-resistance metal contacts to encapsulated semiconductor monolayers with long transfer length. *Nat. Electron.* **5**, 579–585 (2022).

42. T. Uwanno, Y. Hattori, T. Taniguchi, K. Watanabe, K. Nagashio, Fully dry PMMA transfer of graphene on *h*-BN using a heating/cooling system. *2D Mater.* **2**, 041002 (2015).

43. A. Rogalski, Scaling infrared detectors—Status and outlook. *Rep. Prog. Phys.* **85**, 126501 (2022).

44. R. Dagan, Y. Vaknin, A. Henning, J. Y. Shang, L. J. Lauhon, Y. Rosenwaks, Two-dimensional charge carrier distribution in MoS2 monolayer and multilayers. *Appl. Phys. Lett.* **114**, 101602 (2019).

45. T. Li, W. Guo, L. Ma, W. Li, Z. Yu, Z. Han, S. Gao, L. Liu, D. Fan, Z. Wang, Y. Yang, W. Lin, Z. Luo, X. Chen, N. Dai, X. Tu, D. Pan, Y. Yao, P. Wang, Y. Nie, J. Wang, Y. Shi, X. Wang, Epitaxial growth of wafer-scale molybdenum disulfide semiconductor single crystals on sapphire. *Nat. Nanotechnol.* **16**, 1201–1207 (2021).

46. Y. Liu, X. Duan, H.-J. Shin, S. Park, Y. Huang, X. Duan, Promises and prospects of two-dimensional transistors. *Nature* **591**, 43–53 (2021).

47. P. Wang, S. Liu, W. Luo, H. Fang, F. Gong, N. Guo, Z.-G. Chen, J. Zou, Y. Huang, X. Zhou, J. Wang, X. Chen, W. Lu, F. Xiu, W. Hu, Arrayed van der Waals broadband detectors for dual-band detection. *Adv. Mater.* **29**, 1604439 (2017).

48. Y. Jeon, J. Seo, J. Kim, D. Rhee, M. Jung, H. Park, J. Kang, Wafer-scale two-dimensional molybdenum diselenide phototransistor array via liquid-precursor-assisted chemical vapor deposition. *Adv. Opt. Mater.* **10**, 2101492 (2022).

49. A. Bala, M. Sritharan, N. Liu, M. Naqi, A. Sen, G. Han, H. Y. Rho, Y. Yoon, S. Kim, Active pixel image sensor array for dual vision using large-area bilayer WS2. *InfoMat* **6**, e12513 (2024).

50. K. Y. Thai, I. Park, B. J. Kim, A. T. Hoang, Y. Na, C. U. Park, Y. Chae, J.-H. Ahn, MoS2/graphene photodetector array with strain-modulated photoresponse up to the near-infrared regime. *ACS Nano* **15**, 12836–12846 (2021).

51. D. Geum, S. Kim, J. Khym, J. Lim, S. Kim, S. Ahn, T. S. Kim, K. Kang, S. Kim, Arrayed MoS2-In0.53Ga0.47As van der Waals heterostructure for high-speed and broadband detection from visible to shortwave-infrared light. *Small* **17**, e2007357 (2021).

52. R. K. Saroj, P. Guha, S. Lee, D. Yoo, E. Lee, J. Lee, M. Kim, G. Yi, Photodetector arrays based on MBE-grown GaSe/graphene heterostructure. *Adv. Opt. Mater.* **10**, 2200332 (2022).

53. Y. Lu, Y. Wang, C. Xu, C. Xie, W. Li, J. Ding, W. Zhou, Z. Qin, X. Shen, L.-B. Luo, Construction of PtSe2/Ge heterostructure-based short-wavelength infrared photodetector array for image sensing and optical communication applications. *Nanoscale* **13**, 7606–7612 (2021).

54. P. Li, H. Wang, M. Yu, Y. Li, Overview of image smoothing algorithms. *J. Phys. Conf. Ser.* **1883**, 012024 (2021).

55. S. Nakariyakul, Fast spatial averaging: An efficient algorithm for 2D mean filtering. *J. Supercomput.* **65**, 262–273 (2013).

56. A. Makandar, B. Halalli, Image enhancement techniques using highpass and lowpass filters. *Int. J. Comput. Appl.* **109**, 21–27 (2015).

57. X. Liu, X. Lu, H. Shen, Q. Yuan, Y. Jiao, L. Zhang, Stripe noise separation and removal in remote sensing images by consideration of the global sparsity and local variational properties. *IEEE Trans. Geosci. Remote Sens.* **54**, 3049–3060 (2016).

58. P. Jagalingam, A. V. Hegde, A review of quality metrics for fused image. *Aquat. Procedia* **4**, 133–142 (2015).

59. U. Sara, M. Akter, M. S. Uddin, Image quality assessment through FSIM, SSIM, MSE and PSNR—A comparative study. *J. Comput. Commun.* **07**, 8–18 (2019).

60. Z. Wu, Y. Lyu, Y. Zhang, R. Ding, B. Zheng, Z. Yang, S. P. Lau, X. H. Chen, J. Hao, Large-scale growth of few-layer two-dimensional black phosphorus. *Nat. Mater.* **20**, 1203–1209 (2021).

61. C. Chen, Y. Yin, R. Zhang, Q. Yuan, Y. Xu, Y. Zhang, J. Chen, Y. Zhang, C. Li, J. Wang, J. Li, L. Fei, Q. Yu, Z. Zhou, H. Zhang, R. Cheng, Z. Dong, X. Xu, A. Pan, K. Zhang, J. He, Growth of single-crystal black phosphorus and its alloy films through sustained feedstock release. *Nat. Mater.* **22**, 717–724 (2023).

62. Z. Shi, X. Ren, H. Qiao, R. Cao, Y. Zhang, X. Qi, H. Zhang, Recent insights into the robustness of two-dimensional black phosphorous in optoelectronic applications. *J. Photochem. Photobiol. C Photochem. Rev.* **43**, 100354 (2020).

63. M. Peng, R. Xie, Z. Wang, P. Wang, F. Wang, H. Ge, Y. Wang, F. Zhong, P. Wu, J. Ye, Q. Li, L. Zhang, X. Ge, Y. Ye, Y. Lei, W. Jiang, Z. Hu, F. Wu, X. Zhou, J. Miao, J. Wang, H. Yan, C. Shan, J. Dai, C. Chen, X. Chen, W. Lu, W. Hu, Blackbody-sensitive room-temperature

infrared photodetectors based on low-dimensional tellurium grown by chemical vapor deposition. *Sci. Adv.* **7**, eabf7358 (2021).

64. L. Tong, X. Huang, P. Wang, L. Ye, M. Peng, L. An, Q. Sun, Y. Zhang, G. Yang, Z. Li, F. Zhong, F. Wang, Y. Wang, M. Motlag, W. Wu, G. J. Cheng, W. Hu, Stable mid-infrared polarization imaging based on quasi-2D tellurium at room temperature. *Nat. Commun.* **11**, 2308 (2020).

65. G. Kresse, J. Furthmüller, Efficient iterative schemes for ab initio total-energy calculations using a plane-wave basis set. *Phys. Rev. B* **54**, 11169–11186 (1996).

66. G. Kresse, J. Furthmüller, Efficiency of ab-initio total energy calculations for metals and semiconductors using a plane-wave basis set. *Comput. Mater. Sci.* **6**, 15–50 (1996).

67. P. E. Blöchl, Projector augmented-wave method. *Phys. Rev. B* **50**, 17953–17979 (1994).

68. J. P. Perdew, K. Burke, M. Ernzerhof, Generalized gradient approximation made simple. *Phys. Rev. Lett.* **77**, 3865–3868 (1996).

69. S. Grimme, J. Antony, S. Ehrlich, H. Krieg, A consistent and accurate *ab initio* parametrization of density functional dispersion correction (DFT-D) for the 94 elements H-Pu. *J. Chem. Phys.* **132**, 154104 (2010).

70. T. Wang, R. Wang, P. Yuan, S. Xu, J. Liu, X. Wang, Interfacial thermal conductance between mechanically exfoliated black phosphorus and SiO*x* : Effect of thickness and temperature. *Adv. Mater. Interfaces* **4**, 1700233 (2017).

71. P. K. Saxena, Numerical study of dual band (MW/LW) IR detector for performance improvement. *Def. Sci. J.* **67**, 141–148 (2017).

72. A. Rogalski, *Infrared Detectors* (Taylor & Francis, 2nd ed., 2011).

73. F. Wu, Q. Li, P. Wang, H. Xia, Z. Wang, Y. Wang, M. Luo, L. Chen, F. Chen, J. Miao, X. Chen, W. Lu, C. Shan, A. Pan, X. Wu, W. Ren, D. Jariwala, W. Hu, High efficiency and fast van der Waals hetero-photodiodes with a unilateral depletion region. *Nat. Commun.* **10**, 4663 (2019).

74. D. Wu, R. Tian, P. Lin, Z. Shi, X. Chen, M. Jia, Y. Tian, X. Li, L. Zeng, J. Jie, Wafer-scale synthesis of wide bandgap 2D GeSe2 layers for self-powered ultrasensitive UV photodetection and imaging. *Nano Energy* **104**, 107972 (2022).

75. X.-W. Tong, Y.-N. Lin, R. Huang, Z.-X. Zhang, C. Fu, D. Wu, L.-B. Luo, Z.-J. Li, F.-X. Liang, W. Zhang, Direct tellurization of Pt to synthesize 2D PtTe2 for high-performance broadband photodetectors and NIR image sensors. *ACS Appl. Mater. Interfaces* **12**, 53921–53931 (2020).

76. S. J. R. Tan, I. Abdelwahab, L. Chu, S. M. Poh, Y. Liu, J. Lu, W. Chen, K. P. Loh, Quasi-monolayer black phosphorus with high mobility and air stability. *Adv. Mater.* **30**, 1704619 (2018).

77. G. Long, D. Maryenko, J. Shen, S. Xu, J. Hou, Z. Wu, W. K. Wong, T. Han, J. Lin, Y. Cai, R. Lortz, N. Wang, Achieving ultrahigh carrier mobility in two-dimensional hole gas of black phosphorus. *Nano Lett.* **16**, 7768–7773 (2016).

78. Y. Zhao, H. Wang, H. Huang, Q. Xiao, Y. Xu, Z. Guo, H. Xie, J. Shao, Z. Sun, W. Han, X. Yu, P. Li, P. K. Chu, Surface coordination of black phosphorus for robust air and water stability. *Angew. Chem. Int. Ed.* **55**, 5003–5007 (2016).

79. J. D. Wood, S. A. Wells, D. Jariwala, K.-S. Chen, E. Cho, V. K. Sangwan, X. Liu, L. J. Lauhon, T. J. Marks, M. C. Hersam, Effective passivation of exfoliated black phosphorus transistors against ambient degradation. *Nano Lett.* **14**, 6964–6970 (2014).

80. G. Qiu, C. Niu, Y. Wang, M. Si, Z. Zhang, W. Wu, P. D. Ye, Quantum hall effect of Weyl fermions in n-type semiconducting tellurene. *Nat. Nanotechnol.* **15**, 585–591 (2020).

81. L. Liu, T. Li, L. Ma, W. Li, S. Gao, W. Sun, R. Dong, X. Zou, D. Fan, L. Shao, C. Gu, N. Dai, Z. Yu, X. Chen, X. Tu, Y. Nie, P. Wang, J. Wang, Y. Shi, X. Wang, Uniform nucleation and epitaxy of bilayer molybdenum disulfide on sapphire. *Nature* **605**, 69–75 (2022).

82. X. Xu, Y. Pan, S. Liu, B. Han, P. Gu, S. Li, W. Xu, Y. Peng, Z. Han, J. Chen, P. Gao, Y. Ye, Seeded 2D epitaxy of large-area single-crystal films of the van der Waals semiconductor 2H MoTe2. *Science* **372**, 195–200 (2021).

83. M. Peng, Y. Yu, Z. Wang, X. Fu, Y. Gu, Y. Wang, K. Zhang, Z. Zhang, M. Huang, Z. Cui, F. Zhong, P. Wu, J. Ye, T. Xu, Q. Li, P. Wang, F. Yue, F. Wu, J. Dai, C. Chen, W. Hu, Room-temperature blackbody-sensitive and fast infrared photodetectors based on 2D tellurium/graphene Van der Waals heterojunction. *ACS Photonics* **9**, 1775–1782 (2022).

84. Y. Wu, S.-E. Wu, J. Hei, L. Zeng, P. Lin, Z. Shi, Q. Chen, X. Li, X. Yu, D. Wu, Van der Waals integration inch-scale 2D MoSe2 layers on Si for highly-sensitive broadband photodetection and imaging. *Nano Res.* **16**, 11422–11429 (2023).

85. Y. Liu, H. Hu, M. Yuan, H. Yin, Y. Qu, Y. Tan, F. Chen, Red-sensitive image array based on defect-engineered PBDB-T/WSe1.5-WSe2/graphene heterostructure. *Adv. Electron. Mater.* **9**, 2300115 (2023).

86. Y. Gong, P. Xie, X. Xing, Z. Lv, T. Xie, S. Zhu, H. Hsu, Y. Zhou, S. Han, Bioinspired artificial visual system based on 2D WSe2 synapse array. *Adv. Funct. Mater.* **33**, 2303539 (2023).

87. Y.-C. Chen, Y.-J. Lu, Q. Liu, C.-N. Lin, J. Guo, J.-H. Zang, Y.-Z. Tian, C.-X. Shan, Ga2O3 photodetector arrays for solar-blind imaging. *J. Mater. Chem. C* **7**, 2557–2562 (2019).

88. T. Wang, D. Zheng, K. Vegso, N. Mrkyvkova, P. Siffalovic, T. Pauporté, High-resolution and stable ruddlesden–popper quasi-2D perovskite flexible photodetectors arrays for potential applications as optical image sensor. *Adv. Funct. Mater.* **33**, 2304659 (2023).

89. H. Wang, L. Li, J. Ma, J. Li, D. Li, 2D perovskite narrowband photodetector arrays. *J. Mater. Chem. C* **9**, 11085–11090 (2021).

90. Z. Zhang, C. Xu, C. Zhu, X. Tong, C. Fu, J. Wang, Y. Cheng, L. Luo, Fabrication of MAPbI3 perovskite/Si heterojunction photodetector arrays for image sensing application. *Sens. Actuators Phys.* **332**, 113176 (2021).

REFERENCES AND NOTES

1. F. Xia, H. Wang, D. Xiao, M. Dubey, A. Ramasubramaniam, Two-dimensional material nanophotonics. *Nat. Photonics* **8**, 899–907 (2014).

2. F. H. L. Koppens, T. Mueller, Ph. Avouris, A. C. Ferrari, M. S. Vitiello, M. Polini, Photodetectors based on graphene, other two-dimensional materials and hybrid systems. *Nat. Nanotechnol.* **9**, 780–793 (2014).

3. N. Huo, G. Konstantatos, Recent progress and future prospects of 2D-based photodetectors. *Adv. Mater.* **30**, e1801164 (2018).

4. A. Soibel, D. Z. Ting, C. J. Hill, A. M. Fisher, L. Hoglund, S. A. Keo, S. D. Gunapala, Mid-wavelength infrared InAsSb/InSb nBn detector with extended cut-off wavelength. *Appl. Phys. Lett.* **109**, 103505 (2016).

5. Y. Wang, Y. Gu, A. Cui, Q. Li, T. He, K. Zhang, Z. Wang, Z. Li, Z. Zhang, P. Wu, R. Xie, F. Wang, P. Wang, C. Shan, H. Li, Z. Ye, P. Zhou, W. Hu, Fast uncooled mid-wavelength infrared photodetectors with heterostructures of van der Waals on epitaxial HgCdTe. *Adv. Mater.* **34**, e2107772 (2022).

6. D. Alshahrani, M. Kesaria, J. J. Jiménez, D. Kwan, V. Srivastava, M. Delmas, F. M. Morales, B. Liang, D. Huffaker, Effect of interfacial schemes on the optical and structural properties of InAs/GaSb type-II superlattices. *ACS Appl. Mater. Interfaces* **15**, 8624–8635 (2023).

7. A. Rogalski, Progress in focal plane array technologies. *Prog. Quantum Electron.* **36**, 342–473 (2012).

8. Y. Xie, B. Zhang, S. Wang, D. Wang, A. Wang, Z. Wang, H. Yu, H. Zhang, Y. Chen, M. Zhao, B. Huang, L. Mei, J. Wang, Ultrabroadband MoS2 photodetector with spectral response from 445 to 2717 nm. *Adv. Mater.* **29**, 1605972 (2017).

9. W. Li, L. Liu, Q. Tao, Y. Chen, Z. Lu, L. Kong, W. Dang, W. Zhang, Z. Li, Q. Li, J. Tang, L. Ren, W. Song, X. Duan, C. Ma, Y. Xiang, L. Liao, Y. Liu, Realization of ultra-scaled MoS2 vertical diodes via double-side electrodes lamination. *Nano Lett.* **22**, 4429, 4436(2022).

10. N. Huo, G. Konstantatos, Ultrasensitive all-2D MoS2 phototransistors enabled by an out-of-plane MoS2 PN homojunction. *Nat. Commun.* **8**, 572 (2017).

11. F. Zhong, J. Ye, T. He, L. Zhang, Z. Wang, Q. Li, B. Han, P. Wang, P. Wu, Y. Yu, J. Guo, Z. Zhang, M. Peng, T. Xu, X. Ge, Y. Wang, H. Wang, M. Zubair, X. Zhou, P. Gao, Z. Fan, W. Hu, Substitutionally doped MoSe2 for high-performance electronics and optoelectronics. *Small* **17**, e2102855 (2021).

12. A. Varghese, D. Saha, K. Thakar, V. Jindal, S. Ghosh, N. V. Medhekar, S. Ghosh, S. Lodha, Near-direct bandgap WSe2/ReS2 type-II pn heterojunction for enhanced ultrafast photodetection and high-performance photovoltaics. *Nano Lett.* **20**, 1707–1717 (2020).

13. D. Jariwala, V. K. Sangwan, C.-C. Wu, P. L. Prabhumirashi, M. L. Geier, T. J. Marks, L. J. Lauhon, M. C. Hersam, Gate-tunable carbon nanotube–MoS2 heterojunction p-n diode. *Proc. Natl. Acad. Sci. U.S.A.* **110**, 18076–18080 (2013).

14. Y. Wen, L. Yin, P. He, Z. Wang, X. Zhang, Q. Wang, T. A. Shifa, K. Xu, F. Wang, X. Zhan, F. Wang, C. Jiang, J. He, Integrated high-performance infrared phototransistor arrays composed of nonlayered PbS–MoS2 heterostructures with edge contacts. *Nano Lett.* **16**, 6437–6444 (2016).

15. S. Hong, N. Zagni, S. Choo, N. Liu, S. Baek, A. Bala, H. Yoo, B. H. Kang, H. J. Kim, H. J. Yun, M. A. Alam, S. Kim, Highly sensitive active pixel image sensor array driven by large-area bilayer MoS2 transistor circuitry. *Nat. Commun.* **12**, 3559 (2021).

16. B. Sun, L. Kong, G. Li, Q. Su, X. Zhang, Z. Liu, Y. Peng, G. Liao, T. Shi, Fully integrated photodetector array based on an electrochemically exfoliated, atomically thin MoS2 film for photoimaging. *ACS Appl. Electron. Mater.* **4**, 1010–1018 (2022).

17. Q. Zhu, Y. Chen, X. Zhu, Y. Sun, Z. Cheng, J. Xu, M. Xu, High-performance near-infrared PtSe2/n-Ge heterojunction photodetector with ultrathin Al2O3 passivation interlayer. *Sci. China Mater.* **66**, 2777–2787 (2023).

18. L. Zeng, D. Wu, J. Jie, X. Ren, X. Hu, S. P. Lau, Y. Chai, Y. H. Tsang, Van der Waals epitaxial growth of mosaic-like 2D platinum ditelluride layers for room-temperature mid-infrared photodetection up to 10.6 μm. *Adv. Mater.* **32**, e2004412 (2020).

19. L. Li, Y. Yu, G. J. Ye, Q. Ge, X. Ou, H. Wu, D. Feng, X. H. Chen, Y. Zhang, Black phosphorus field-effect transistors. *Nat. Nanotechnol.* **9**, 372–377 (2014).

20. M. Amani, E. Regan, J. Bullock, G. H. Ahn, A. Javey, Mid-wave infrared photoconductors based on black phosphorus-arsenic alloys. *ACS Nano* **11**, 11724–11731 (2017).

21. H. Yuan, X. Liu, F. Afshinmanesh, W. Li, G. Xu, J. Sun, B. Lian, A. G. Curto, G. Ye, Y. Hikita, Z. Shen, S.-C. Zhang, X. Chen, M. Brongersma, H. Y. Hwang, Y. Cui, Polarization-sensitive broadband photodetector using a black phosphorus vertical p–n junction. *Nat. Nanotechnol.* **10**, 707–713 (2015).

22. J. Bullock, M. Amani, J. Cho, Y.-Z. Chen, G. H. Ahn, V. Adinolfi, V. R. Shrestha, Y. Gao, K. B. Crozier, Y.-L. Chueh, A. Javey, Polarization-resolved black phosphorus/molybdenum disulfide mid-wave infrared photodiodes with high detectivity at room temperature. *Nat. Photonics* **12**, 601–607 (2018).

23. L. Ye, P. Wang, W. Luo, F. Gong, L. Liao, T. Liu, L. Tong, J. Zang, J. Xu, W. Hu, Highly polarization sensitive infrared photodetector based on black phosphorus-on-WSe2 photogate vertical heterostructure. *Nano Energy* **37**, 53–60 (2017).

24. S. Lee, R. Peng, C. Wu, M. Li, Programmable black phosphorus image sensor for broadband optoelectronic edge computing. *Nat. Commun.* **13**, 1485 (2022).

25. H. Kim, S. Z. Uddin, D.-H. Lien, M. Yeh, N. S. Azar, S. Balendhran, T. Kim, N. Gupta, Y. Rho, C. P. Grigoropoulos, K. B. Crozier, A. Javey, Actively variable-spectrum optoelectronics with black phosphorus. *Nature* **596**, 232–237 (2021).

26. S. Yuan, D. Naveh, K. Watanabe, T. Taniguchi, F. Xia, A wavelength-scale black phosphorus spectrometer. *Nat. Photonics* **15**, 601–607 (2021).

27. Y. Chen, Y. Wang, Z. Wang, Y. Gu, Y. Ye, X. Chai, J. Ye, Y. Chen, R. Xie, Y. Zhou, Z. Hu, Q. Li, L. Zhang, F. Wang, P. Wang, J. Miao, J. Wang, X. Chen, W. Lu, P. Zhou, W. Hu, Unipolar barrier photodetectors based on van der Waals heterostructures. *Nat. Electron.* **4**, 357–363 (2021).

28. P. Wu, L. Ye, L. Tong, P. Wang, Y. Wang, H. Wang, H. Ge, Z. Wang, Y. Gu, K. Zhang, Y. Yu, M. Peng, F. Wang, M. Huang, P. Zhou, W. Hu, Van der Waals two-color infrared photodetector. *Light Sci. Appl.* **11**, 6 (2022).

29. L. Ye, H. Li, Z. Chen, J. Xu, Near-infrared photodetector based on MoS2/black phosphorus heterojunction. *ACS Photonics* **3**, 692–699 (2016).

30. C. R. Dean, A. F. Young, I. Meric, C. Lee, L. Wang, S. Sorgenfrei, K. Watanabe, T. Taniguchi, P. Kim, K. L. Shepard, J. Hone, Boron nitride substrates for high-quality graphene electronics. *Nat. Nanotechnol.* **5**, 722–726 (2010).

31. H. Jawa, A. Varghese, S. Ghosh, S. Sahoo, Y. Yin, N. V. Medhekar, S. Lodha, Wavelength-controlled photocurrent polarity switching in BP-MoS2 heterostructure. *Adv. Funct. Mater.* **32**, 2112696 (2022).

32. X. Chen, X. Lu, B. Deng, O. Sinai, Y. Shao, C. Li, S. Yuan, V. Tran, K. Watanabe, T. Taniguchi, D. Naveh, L. Yang, F. Xia, Widely tunable black phosphorus mid-infrared photodetector. *Nat. Commun.* **8**, 1672 (2017).

33. L. Tao, H. Li, Y. Gao, Z. Chen, L. Wang, Y. Deng, J. Zhang, J. Xu, Deterministic and etching-free transfer of large-scale 2D layered materials for constructing interlayer coupled van der Waals heterostructures. *Adv. Mater. Technol.* **3**, 1700282 (2018).

34. D. G. Purdie, N. M. Pugno, T. Taniguchi, K. Watanabe, A. C. Ferrari, A. Lombardo, Cleaning interfaces in layered materials heterostructures. *Nat. Commun.* **9**, 5387 (2018).

35. K. Kinoshita, R. Moriya, M. Onodera, Y. Wakafuji, S. Masubuchi, K. Watanabe, T. Taniguchi, T. Machida, Dry release transfer of graphene and few-layer h-BN by utilizing thermoplasticity of polypropylene carbonate. *NPJ 2D Mater. Appl.* **3**, 22 (2019).

36. T. Iwasaki, K. Endo, E. Watanabe, D. Tsuya, Y. Morita, S. Nakaharai, Y. Noguchi, Y. Wakayama, K. Watanabe, T. Taniguchi, S. Moriyama, Bubble-free transfer technique for high-quality graphene/hexagonal boron nitride van der Waals heterostructures. *ACS Appl. Mater. Interfaces* **12**, 8533–8538 (2020).

37. J. Chen, L. Liu, H. Chen, N. Xu, S. Deng, Controlled preparation of high quality bubble-free and uniform conducting interfaces of vertical van der Waals heterostructures of arrays. *ACS Appl. Mater. Interfaces* **16**, 10877–10885 (2024).

38. F. Wang, T. Zhang, R. Xie, Z. Wang, W. Hu, How to characterize figures of merit of two-dimensional photodetectors. *Nat. Commun.* **14**, 2224 (2023).

39. G.-X. Ni, Y. Zheng, S. Bae, H. R. Kim, A. Pachoud, Y. S. Kim, C.-L. Tan, D. Im, J.-H. Ahn, B. H. Hong, B. Özyilmaz, Quasi-periodic nanoripples in graphene grown by chemical vapor deposition and its impact on charge transport. *ACS Nano* **6**, 1158–1164 (2012).

40. H. Fang, W. Hu, Photogating in low dimensional photodetectors. *Adv. Sci.* **4**, 1700323 (2017).

41. Y. Liu, S. Liu, Z. Wang, B. Li, K. Watanabe, T. Taniguchi, W. J. Yoo, J. Hone, Low-resistance metal contacts to encapsulated semiconductor monolayers with long transfer length. *Nat. Electron.* **5**, 579–585 (2022).

42. T. Uwanno, Y. Hattori, T. Taniguchi, K. Watanabe, K. Nagashio, Fully dry PMMA transfer of graphene on *h*-BN using a heating/cooling system. *2D Mater.* **2**, 041002 (2015).

43. A. Rogalski, Scaling infrared detectors—Status and outlook. *Rep. Prog. Phys.* **85**, 126501 (2022).

44. R. Dagan, Y. Vaknin, A. Henning, J. Y. Shang, L. J. Lauhon, Y. Rosenwaks, Two-dimensional charge carrier distribution in MoS2 monolayer and multilayers. *Appl. Phys. Lett.* **114**, 101602 (2019).

45. T. Li, W. Guo, L. Ma, W. Li, Z. Yu, Z. Han, S. Gao, L. Liu, D. Fan, Z. Wang, Y. Yang, W. Lin, Z. Luo, X. Chen, N. Dai, X. Tu, D. Pan, Y. Yao, P. Wang, Y. Nie, J. Wang, Y. Shi, X. Wang, Epitaxial growth of wafer-scale molybdenum disulfide semiconductor single crystals on sapphire. *Nat. Nanotechnol.* **16**, 1201–1207 (2021).

46. Y. Liu, X. Duan, H.-J. Shin, S. Park, Y. Huang, X. Duan, Promises and prospects of two-dimensional transistors. *Nature* **591**, 43–53 (2021).

47. P. Wang, S. Liu, W. Luo, H. Fang, F. Gong, N. Guo, Z.-G. Chen, J. Zou, Y. Huang, X. Zhou, J. Wang, X. Chen, W. Lu, F. Xiu, W. Hu, Arrayed van der Waals broadband detectors for dual-band detection. *Adv. Mater.* **29**, 1604439 (2017).

48. Y. Jeon, J. Seo, J. Kim, D. Rhee, M. Jung, H. Park, J. Kang, Wafer-scale two-dimensional molybdenum diselenide phototransistor array via liquid-precursor-assisted chemical vapor deposition. *Adv. Opt. Mater.* **10**, 2101492 (2022).

49. A. Bala, M. Sritharan, N. Liu, M. Naqi, A. Sen, G. Han, H. Y. Rho, Y. Yoon, S. Kim, Active pixel image sensor array for dual vision using large-area bilayer WS2. *InfoMat* **6**, e12513 (2024).

50. K. Y. Thai, I. Park, B. J. Kim, A. T. Hoang, Y. Na, C. U. Park, Y. Chae, J.-H. Ahn, MoS2/graphene photodetector array with strain-modulated photoresponse up to the near-infrared regime. *ACS Nano* **15**, 12836–12846 (2021).

51. D. Geum, S. Kim, J. Khym, J. Lim, S. Kim, S. Ahn, T. S. Kim, K. Kang, S. Kim, Arrayed MoS2-In0.53Ga0.47As van der Waals heterostructure for high-speed and broadband detection from visible to shortwave-infrared light. *Small* **17**, e2007357 (2021).

52. R. K. Saroj, P. Guha, S. Lee, D. Yoo, E. Lee, J. Lee, M. Kim, G. Yi, Photodetector arrays based on MBE-grown GaSe/graphene heterostructure. *Adv. Opt. Mater.* **10**, 2200332 (2022).

53. Y. Lu, Y. Wang, C. Xu, C. Xie, W. Li, J. Ding, W. Zhou, Z. Qin, X. Shen, L.-B. Luo, Construction of PtSe2/Ge heterostructure-based short-wavelength infrared photodetector array for image sensing and optical communication applications. *Nanoscale* **13**, 7606–7612 (2021).

54. P. Li, H. Wang, M. Yu, Y. Li, Overview of image smoothing algorithms. *J. Phys. Conf. Ser.* **1883**, 012024 (2021).

55. S. Nakariyakul, Fast spatial averaging: An efficient algorithm for 2D mean filtering. *J. Supercomput.* **65**, 262–273 (2013).

56. A. Makandar, B. Halalli, Image enhancement techniques using highpass and lowpass filters. *Int. J. Comput. Appl.* **109**, 21–27 (2015).

57. X. Liu, X. Lu, H. Shen, Q. Yuan, Y. Jiao, L. Zhang, Stripe noise separation and removal in remote sensing images by consideration of the global sparsity and local variational properties. *IEEE Trans. Geosci. Remote Sens.* **54**, 3049–3060 (2016).

58. P. Jagalingam, A. V. Hegde, A review of quality metrics for fused image. *Aquat. Procedia* **4**, 133–142 (2015).

59. U. Sara, M. Akter, M. S. Uddin, Image quality assessment through FSIM, SSIM, MSE and PSNR—A comparative study. *J. Comput. Commun.* **07**, 8–18 (2019).

60. Z. Wu, Y. Lyu, Y. Zhang, R. Ding, B. Zheng, Z. Yang, S. P. Lau, X. H. Chen, J. Hao, Large-scale growth of few-layer two-dimensional black phosphorus. *Nat. Mater.* **20**, 1203–1209 (2021).

61. C. Chen, Y. Yin, R. Zhang, Q. Yuan, Y. Xu, Y. Zhang, J. Chen, Y. Zhang, C. Li, J. Wang, J. Li, L. Fei, Q. Yu, Z. Zhou, H. Zhang, R. Cheng, Z. Dong, X. Xu, A. Pan, K. Zhang, J. He, Growth of single-crystal black phosphorus and its alloy films through sustained feedstock release. *Nat. Mater.* **22**, 717–724 (2023).

62. Z. Shi, X. Ren, H. Qiao, R. Cao, Y. Zhang, X. Qi, H. Zhang, Recent insights into the robustness of two-dimensional black phosphorous in optoelectronic applications. *J. Photochem. Photobiol. C Photochem. Rev.* **43**, 100354 (2020).

63. M. Peng, R. Xie, Z. Wang, P. Wang, F. Wang, H. Ge, Y. Wang, F. Zhong, P. Wu, J. Ye, Q. Li, L. Zhang, X. Ge, Y. Ye, Y. Lei, W. Jiang, Z. Hu, F. Wu, X. Zhou, J. Miao, J. Wang, H. Yan, C. Shan, J. Dai, C. Chen, X. Chen, W. Lu, W. Hu, Blackbody-sensitive room-temperature

infrared photodetectors based on low-dimensional tellurium grown by chemical vapor deposition. *Sci. Adv.* **7**, eabf7358 (2021).

64. L. Tong, X. Huang, P. Wang, L. Ye, M. Peng, L. An, Q. Sun, Y. Zhang, G. Yang, Z. Li, F. Zhong, F. Wang, Y. Wang, M. Motlag, W. Wu, G. J. Cheng, W. Hu, Stable mid-infrared polarization imaging based on quasi-2D tellurium at room temperature. *Nat. Commun.* **11**, 2308 (2020).

65. G. Kresse, J. Furthmüller, Efficient iterative schemes for ab initio total-energy calculations using a plane-wave basis set. *Phys. Rev. B* **54**, 11169–11186 (1996).

66. G. Kresse, J. Furthmüller, Efficiency of ab-initio total energy calculations for metals and semiconductors using a plane-wave basis set. *Comput. Mater. Sci.* **6**, 15–50 (1996).

67. P. E. Blöchl, Projector augmented-wave method. *Phys. Rev. B* **50**, 17953–17979 (1994).

68. J. P. Perdew, K. Burke, M. Ernzerhof, Generalized gradient approximation made simple. *Phys. Rev. Lett.* **77**, 3865–3868 (1996).

69. S. Grimme, J. Antony, S. Ehrlich, H. Krieg, A consistent and accurate *ab initio* parametrization of density functional dispersion correction (DFT-D) for the 94 elements H-Pu. *J. Chem. Phys.* **132**, 154104 (2010).

70. T. Wang, R. Wang, P. Yuan, S. Xu, J. Liu, X. Wang, Interfacial thermal conductance between mechanically exfoliated black phosphorus and SiO*x* : Effect of thickness and temperature. *Adv. Mater. Interfaces* **4**, 1700233 (2017).

71. P. K. Saxena, Numerical study of dual band (MW/LW) IR detector for performance improvement. *Def. Sci. J.* **67**, 141–148 (2017).

72. A. Rogalski, *Infrared Detectors* (Taylor & Francis, 2nd ed., 2011).

73. F. Wu, Q. Li, P. Wang, H. Xia, Z. Wang, Y. Wang, M. Luo, L. Chen, F. Chen, J. Miao, X. Chen, W. Lu, C. Shan, A. Pan, X. Wu, W. Ren, D. Jariwala, W. Hu, High efficiency and fast van der Waals hetero-photodiodes with a unilateral depletion region. *Nat. Commun.* **10**, 4663 (2019).

74. D. Wu, R. Tian, P. Lin, Z. Shi, X. Chen, M. Jia, Y. Tian, X. Li, L. Zeng, J. Jie, Wafer-scale synthesis of wide bandgap 2D GeSe2 layers for self-powered ultrasensitive UV photodetection and imaging. *Nano Energy* **104**, 107972 (2022).

75. X.-W. Tong, Y.-N. Lin, R. Huang, Z.-X. Zhang, C. Fu, D. Wu, L.-B. Luo, Z.-J. Li, F.-X. Liang, W. Zhang, Direct tellurization of Pt to synthesize 2D PtTe2 for high-performance broadband photodetectors and NIR image sensors. *ACS Appl. Mater. Interfaces* **12**, 53921–53931 (2020).

76. S. J. R. Tan, I. Abdelwahab, L. Chu, S. M. Poh, Y. Liu, J. Lu, W. Chen, K. P. Loh, Quasi-monolayer black phosphorus with high mobility and air stability. *Adv. Mater.* **30**, 1704619 (2018).

77. G. Long, D. Maryenko, J. Shen, S. Xu, J. Hou, Z. Wu, W. K. Wong, T. Han, J. Lin, Y. Cai, R. Lortz, N. Wang, Achieving ultrahigh carrier mobility in two-dimensional hole gas of black phosphorus. *Nano Lett.* **16**, 7768–7773 (2016).

78. Y. Zhao, H. Wang, H. Huang, Q. Xiao, Y. Xu, Z. Guo, H. Xie, J. Shao, Z. Sun, W. Han, X. Yu, P. Li, P. K. Chu, Surface coordination of black phosphorus for robust air and water stability. *Angew. Chem. Int. Ed.* **55**, 5003–5007 (2016).

79. J. D. Wood, S. A. Wells, D. Jariwala, K.-S. Chen, E. Cho, V. K. Sangwan, X. Liu, L. J. Lauhon, T. J. Marks, M. C. Hersam, Effective passivation of exfoliated black phosphorus transistors against ambient degradation. *Nano Lett.* **14**, 6964–6970 (2014).

80. G. Qiu, C. Niu, Y. Wang, M. Si, Z. Zhang, W. Wu, P. D. Ye, Quantum hall effect of Weyl fermions in n-type semiconducting tellurene. *Nat. Nanotechnol.* **15**, 585–591 (2020).

81. L. Liu, T. Li, L. Ma, W. Li, S. Gao, W. Sun, R. Dong, X. Zou, D. Fan, L. Shao, C. Gu, N. Dai, Z. Yu, X. Chen, X. Tu, Y. Nie, P. Wang, J. Wang, Y. Shi, X. Wang, Uniform nucleation and epitaxy of bilayer molybdenum disulfide on sapphire. *Nature* **605**, 69–75 (2022).

82. X. Xu, Y. Pan, S. Liu, B. Han, P. Gu, S. Li, W. Xu, Y. Peng, Z. Han, J. Chen, P. Gao, Y. Ye, Seeded 2D epitaxy of large-area single-crystal films of the van der Waals semiconductor 2H MoTe2. *Science* **372**, 195–200 (2021).

83. M. Peng, Y. Yu, Z. Wang, X. Fu, Y. Gu, Y. Wang, K. Zhang, Z. Zhang, M. Huang, Z. Cui, F. Zhong, P. Wu, J. Ye, T. Xu, Q. Li, P. Wang, F. Yue, F. Wu, J. Dai, C. Chen, W. Hu, Room-temperature blackbody-sensitive and fast infrared photodetectors based on 2D tellurium/graphene Van der Waals heterojunction. *ACS Photonics* **9**, 1775–1782 (2022).

84. Y. Wu, S.-E. Wu, J. Hei, L. Zeng, P. Lin, Z. Shi, Q. Chen, X. Li, X. Yu, D. Wu, Van der Waals integration inch-scale 2D MoSe2 layers on Si for highly-sensitive broadband photodetection and imaging. *Nano Res.* **16**, 11422–11429 (2023).

85. Y. Liu, H. Hu, M. Yuan, H. Yin, Y. Qu, Y. Tan, F. Chen, Red-sensitive image array based on defect-engineered PBDB-T/WSe1.5-WSe2/graphene heterostructure. *Adv. Electron. Mater.* **9**, 2300115 (2023).

86. Y. Gong, P. Xie, X. Xing, Z. Lv, T. Xie, S. Zhu, H. Hsu, Y. Zhou, S. Han, Bioinspired artificial visual system based on 2D WSe2 synapse array. *Adv. Funct. Mater.* **33**, 2303539 (2023).

87. Y.-C. Chen, Y.-J. Lu, Q. Liu, C.-N. Lin, J. Guo, J.-H. Zang, Y.-Z. Tian, C.-X. Shan, Ga2O3 photodetector arrays for solar-blind imaging. *J. Mater. Chem. C* **7**, 2557–2562 (2019).

88. T. Wang, D. Zheng, K. Vegso, N. Mrkyvkova, P. Siffalovic, T. Pauporté, High-resolution and stable ruddlesden–popper quasi-2D perovskite flexible photodetectors arrays for potential applications as optical image sensor. *Adv. Funct. Mater.* **33**, 2304659 (2023).

89. H. Wang, L. Li, J. Ma, J. Li, D. Li, 2D perovskite narrowband photodetector arrays. *J. Mater. Chem. C* **9**, 11085–11090 (2021).

90. Z. Zhang, C. Xu, C. Zhu, X. Tong, C. Fu, J. Wang, Y. Cheng, L. Luo, Fabrication of MAPbI3 perovskite/Si heterojunction photodetector arrays for image sensing application. *Sens. Actuators Phys.* **332**, 113176 (2021).